remote sensing

MDPI

Article

Coastal Vulnerability Index (CVI) Assessment of a Data-Sparse Delta: Quantifying the Contribution of InSAR-Derived Land Subsidence in the Volta Delta, Ghana

Selasi Yao Avornyo [1], Roberta Bonì [2,*], Femi Emmanuel Ikuemonisan [3], Philip-Neri Jayson-Quashigah [4], Obed Omane Okyere [4], Michael Kwame-Biney [1], Philip S. J. Minderhoud [5,6,7], Edem Mahu [1], Pietro Teatini [6] and Kwasi Appeaning Addo [1]

1 Department of Marine and Fisheries Sciences, University of Ghana, Legon, Accra P.O. Box LG 99, Ghana; selavorn@gmail.com (S.Y.A.); mkwame-biney@st.ug.edu.gh (M.K.-B.); emahu@ug.edu.gh (E.M.); kappeaningaddo@ug.edu.gh (K.A.A.)
2 Department of Science, Technology and Society (STS), University School for Advanced Studies (IUSS) Pavia, 27100 Pavia, Italy
3 Department of Physics, Lagos State University of Education, Lagos 100001, Nigeria; ikuemonisanfe@lasued.edu.ng
4 Institute for Environment and Sanitation Studies, University of Ghana, Legon, Accra P.O. Box LG 209, Ghana; pnjquashigah@ug.edu.gh (P.-N.J.-Q.); omaneokyere@ug.edu.gh (O.O.O.)
5 Soil Geography and Landscape Group, Wageningen University, 6708 PB Wageningen, The Netherlands; philip.minderhoud@wur.nl
6 Department of Civil, Environmental and Architectural Engineering, University of Padova, 35131 Padova, Italy; pietro.teatini@unipd.it
7 Department of Subsurface and Groundwater Systems, Deltares Research Institute, 3508 AL Utrecht, The Netherlands
* Correspondence: roberta.boni@iusspavia.it

Highlights

What are the main findings?

- Including measured subsidence, InSAR-derived land subsidence in the Coastal Vulnerability Index raised the mean vulnerability of the Volta Delta's coastline from moderate to very high, with 75% of grid cells rated as high or very high once locally measured subsidence was accounted for, compared with 44% using the regional estimate and 28% when subsidence was left out.
- A mean subsidence rate of about 3.35 mm/yr roughly doubles the local rate of relative sea-level rise against a regional rise of 4 to 5 mm/yr, and the highest vulnerability consistently falls along the lagoonal margins.

What are the implications of the main findings?

- Deltaic coastal vulnerability assessments that assume global average subsidence rates understate the real exposure of subsiding deltas and can misdirect where adaptation funding is placed.
- Where subsidence has an anthropogenic component, it becomes a hazard that can be managed at its source rather than only defended against, especially at the worst hotspots where hard engineering defences risk worsening erosion downdrift and blocking the landward retreat of coastal ecosystems.

Check for updates

Academic Editor: Dongping Ming

Received: 18 July 2026
Revised: 1 September 2026
Accepted: 3 September 2026
Published: 6 September 2026

Copyright: © 2026 by the authors. Licensee MDPI, Basel, Switzerland. This article is an open access article distributed under the terms and conditions of the Creative Commons Attribution (CC BY) license.

Abstract

Land subsidence amplifies the impacts of sea-level rise (SLR) in low-lying deltas, yet some Coastal Vulnerability Index (CVI) assessments omit this or rely on global estimates, drastically understating deltaic vulnerability. This study presents the first CVI assessment

along Ghana's coast to integrate validated, spatially resolved land subsidence derived from Persistent Scatterer Interferometric Synthetic Aperture Radar (PS-InSAR). Nine geological, geomorphological, hydrodynamic, and anthropogenic variables were quantified across 72 contiguous grid cells spanning ~150 km of the Volta Delta's coastline and ranked on a 1–5 vulnerability scale. Three composite indices were computed using a common quantile distribution: an index excluding subsidence (CVI_{-sub}), an index with a spatially uniform regional vertical land motion ($CVI_{+(u\text{-}sub)}$), and an index incorporating spatially resolved local InSAR subsidence ($CVI_{+(v\text{-}sub)}$). High to very high vulnerability ranks rose from 28% of cells without subsidence, through 44% with the regional estimate, to 75% with the local InSAR; every grid cell recorded a higher CVI once subsidence was incorporated (Wilcoxon signed-rank test, $p < 0.001$). Vulnerability peaked along the Keta and Songor lagoonal margins. Omitting measured subsidence understates deltaic vulnerability, and this approach offers a transferable method for data-sparse deltas.

Keywords: Coastal Vulnerability Index (CVI); land subsidence; InSAR; coastal hazards; sea-level rise; Volta Delta; Ghana

1. Introduction

Coastal zones support over two thirds of the global population [1,2] and contribute largely to national economic output through fisheries, tourism, and maritime trade [3]. However, these environments are also among the most exposed to the growing impacts of climate change. Multi-hazards such as coastal erosion, saltwater intrusion, periodic flooding, sea-level rise (SLR), and storm surges are increasing in frequency and intensity, and projections indicate their continued acceleration throughout the 21st century [4]. In low-lying deltaic coastal environments, these multi-hazards are amplified by land subsidence, the downward displacement of the ground surface, which exacerbates the rate of relative SLR experienced at the coast beyond what eustatic global estimates alone would suggest [5–9].

SLR results primarily from the thermal expansion of ocean water and the accelerating loss of ice from glaciers and ice sheets [10]. Since the pre-industrial period, the global mean sea level has risen by approximately 0.20 m, with current rates near 3.6 mm/yr and projections exceeding 1 m by the end of the century (2100) under high-emission scenarios [4]. In coastal areas, SLR accelerates saltwater intrusion into freshwater aquifers [11], leads to permanent inundation of low-lying terrain [12], intensifies storm surge impacts [4], and disrupts healthy coastal ecosystem functions that provide natural protection, including mangroves, wetlands, and beaches [13,14]. In the Global South, where most countries have environment-dependent economies, most low-lying coastal deltas are severely impacted due to limited adaptive capacity [15]. The West African sub-region is no exception to this global phenomenon. The West African coast, which already has a low-elevation coastal zone [3,16], experiences storm surges with high winds and intense wave action that cause coastal erosion [17]. With increasing global temperatures [4], coastal multi-hazards are projected to intensify. Climate projections predict that the West African coastal region may experience more frequent coastal hazards by 2100 [18–20]. Some of these coastal hazards have become prevalent in recent years.

Despite its exacerbating effect, land subsidence receives inadequate attention in coastal vulnerability research, particularly in West Africa [15,21]. Land subsidence is driven by both natural and human-induced factors. However, land subsidence is driven more prominently by human-induced factors, such as sediment compaction [22], groundwater or hydrocarbon extraction [6,23], sediment starvation through damming and coastal infrastructure [8],

local and basin tectonics [24], isostasy [25], natural oxidation, and land drainage [26], amongst others. In most deltaic environments, natural compaction of unconsolidated alluvial deposits is compounded by human activities, producing subsidence rates that far exceed local SLR rates [7,8,26]. Subsidence directly amplifies the local rate of relative SLR, a combination of land subsidence and offshore (eustatic) SLR. Hypothetically, a coast experiencing 5 mm/yr of eustatic SLR and 8 mm/yr of subsidence is effectively experiencing a relative SLR of 13 mm/yr, well above what global tide gauge or satellite altimetry records alone would indicate. Also, the local rates of relative SLR can vary spatio-temporally. Stouthamer and Asselen [27] have noted that the spatio-temporal variability in subsidence corresponds to the natural and human-induced drivers of land deformation, which often manifest at localised scales that are not captured by global estimates.

Understanding the difference between relative and eustatic SLR is critical for accurate coastal vulnerability assessments. The concept of vulnerability is generally expressed in terms of the exposure, sensitivity, and adaptive capacity of a system to climate-related multi-hazards [28]. Among the methodologies employed for evaluating coastal risk, index-based techniques such as the Coastal Vulnerability Index (CVI) have been widely applied due to their simplicity, transparency, and ability to integrate multiple geological and physical process variables into a simple composite measure (e.g., Appeaning Addo [17]; Boateng et al. [29]; Theocharidis et al. [30]). Particularly in the case of Ghana's Volta Delta, which is challenged by data sparsity, the CVI approach fits its data constraints. Other approaches include indicator-based methods [31], Geographic Information System (GIS)-based decision-support systems [32], and dynamic computer models [33].

Due to the large number of parameters that coastal vulnerability assessment entails and their potential interactions, the evaluation is typically approximated and simplified [34]. However, some CVI frameworks either omit subsidence entirely, use spatially uniform rates from distant tidal gauges, or use assumed global averages, typically between −1 and −2 mm/yr (e.g., Appeaning Addo [17]; Boateng et al. [29]), instead of locally measured and spatially resolved rates. In deltaic settings with higher localised subsidence, this approach systematically underestimates actual vulnerability. Interferometric Synthetic Aperture Radar (InSAR), a satellite-based technique, offers a practical solution. InSAR measures ground deformation to the millimetre scale, across varying spatio-temporal scales at relatively low cost, and with validated accuracy in deltaic and coastal settings globally [35,36]. Despite these advantages, InSAR-derived subsidence data remain largely absent from CVI frameworks applied along the West African coast.

Previous CVI assessments along Ghana's coast, such as those by Boateng et al. [29] at the district scale for the entire coast and Appeaning Addo [17] at a sub-regional scale (Accra), have established useful baseline profiles. However, both studies did not use spatially resolved measured data. In a delta where sediment compaction, salt mining, wetland drainage, and groundwater extraction may drive locally variable subsidence, using unresolved spatial data introduces unquantified errors that may alter vulnerability classifications. Boateng et al.'s [29] approximation of land subsidence from a single tide gauge to represent the entire coast, including the Volta Delta despite it being located over 300 km east of the tide gauge, introduces unquantified bias in vulnerability classification. As a knowledge gap identified by Avornyo et al. [15], no spatially resolved InSAR-derived subsidence measurements have been integrated into any CVI assessment for the Volta Delta or any other part of Ghana's coastline. Additionally, the contribution of land subsidence to the delta's overall coastal vulnerability profile, relative to geophysical and oceanographic variables, remains unquantified.

This study therefore seeks to assess the vulnerability of the Volta Delta's coastline using geological, geomorphological, hydrodynamic, and anthropogenic variables, and to

identify coastal hotspots that are highly vulnerable to the impending threats of climate change. Specifically, it addresses these gaps through four objectives: (i) to quantify and rank nine geological, geomorphological, hydrodynamic, and anthropogenic variables across the Volta Delta coastline using a standardised one to five vulnerability classification scheme; (ii) to compute and compare three CVIs—one with the spatially resolved InSAR-derived local vertical land motion (VLM) ($CVI_{+(v\text{-}sub)}$), one with a spatially uniform regional VLM ($CVI_{+(u\text{-}sub)}$), and one excluding VLM ($CVI_{\text{-}sub}$); (iii) to assess the contribution of measured land subsidence to the overall coastal vulnerability classification; and (iv) to identify spatial hotspots of high and very high coastal vulnerability. It is hypothesised that the inclusion of spatially resolved local subsidence rates will significantly increase the vulnerability classification of the Volta Delta.

2. Materials and Methods

2.1. Study Area

The Volta Delta is located in Southeastern Ghana, along the Gulf of Guinea. The delta's coastline stretches approximately 150 km along the coast of the Bight of Benin, extending from the Ghana–Togo border in the east to Ningo–Prampram to the west. The inland extents are delineated by the 5 m elevation contour within the Accra–Ho–Keta plains (Figure 1), covering an area of about 2000 km^2, which is administratively made up of ten (10) districts [5]. The delta is predominantly characterised by low-lying topography, a sandy barrier shoreline, and two extensive lagoonal systems: the Keta lagoon to the east and the Songor lagoon to the west. The delta's coast is bounded by a narrow shelf, varying between 15 and 33 km wide, and is characterised by a relatively uniform, moderately steep shoreface with a gradient ranging between 1:120 and 1:150 down to 15 m, which is considered to be the close-out depth for significant wave-induced sediment movement along its coast [37].

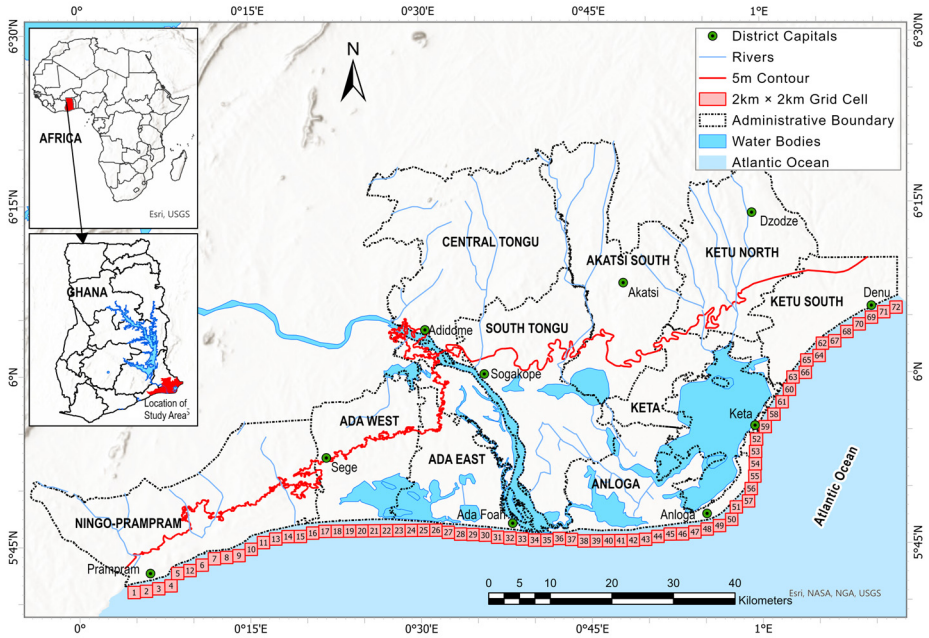


Figure 1. Map of the study area, with the red elevation contour showing the landward delineation of the Volta Delta. The 72 contiguous grid cells (2 km × 2 km) were used in the segmentation and quantification of the CVI.

Geologically, the delta is located within the Keta Basin and includes late quaternary rocks and loose sediments made up of clay, sand, and gravel deposits [15,38]. Acid and basic gneisses and schists of the Dahomeyan system underlie the basin and outcrop on its

northern margins [39]. Large portions of the coastal fringe sit below the 2 m above mean sea level, making them susceptible to inundation from the sea, lagoon, and other inland water bodies [40], along with other multi-hazards, such as erosion and saltwater intrusion into freshwater aquifers. Over time, there have been significant sea defence initiatives, such as the Keta Sea Defence Project, the Dzita–Atorkor Sea Defence, the Ada Sea Defence, the Ningo–Prampram Sea Defence, and, more recently, the makeshift Blekusu–Agavedzi Sea Defence, in response to the destruction caused by coastal erosion along this coast. Even though these initiatives have stabilised the local shoreline, erosion continues, especially at the downdrift of these structures [38]. There is also evidence of land subsidence rates exceeding 8 mm/yr and exacerbating the recurrence of prevalent multi-hazard events [5].

The delta supports livelihoods that include artisanal fisheries, subsistence and commercial agriculture, salt mining and aquaculture [41]. These activities are concentrated along the coastal fringe and lagoonal margins, thereby directly exposing them to multi-hazard events such as erosion, flooding and saltwater intrusion. The Volta Delta is both a scientifically important site for studying low-lying deltaic vulnerability in the Global South and a policy-relevant priority for Ghana's national coastal adaptation planning.

2.2. Methodological Framework

The methodology follows six (6) sequential stages. Stage one covers the acquisition and processing of all variable data from validated sources. Stage two covers the segmentation of the approximately 150 km Volta Delta into 72 contiguous grid cells at 2 km intervals. Stage three covers the quantification of each variable within each cell and the ranking of each variable on a 1 to 5 vulnerability scale. Stage four involves the computation of three composite CVIs: one with the spatially resolved local InSAR subsidence ($CVI_{+(v\text{-}sub)}$), one with a spatially uniform regional VLM ($CVI_{+(u\text{-}sub)}$), and one excluding subsidence ($CVI_{\text{-}sub}$). Stage five covers the classification of CVI values into percentile vulnerability categories and the creation of grid cell vulnerability maps for the three scenarios. Stage six covers the identification of spatial hotspots and statistical analysis. A methodological workflow is provided in Figure 2. The six-stage structure, the three-scenario logic, and the nine-variable set were defined and rendered as a workflow chart with the assistance of Claude (Anthropic; application version v1.11187.5, model Opus 4.8).

2.3. Data Acquisition and Sources

The initial step in computing the CVI is to identify the variables that influence vulnerability. Most of the selected variables were identified by Appeaning Addo et al. [41] as the drivers potentially influencing the vulnerability of Volta Delta's coast. To evaluate the influence of land subsidence on coastal vulnerability, the CVI was computed under the three scenarios. In the first scenario, the CVI was calculated using eight standard variables: shoreline change, geology, coastal slope, geomorphology, mean tidal range, sea-level rise, land cover, and significant wave height. In the second scenario, the spatially resolved InSAR subsidence was incorporated as a ninth variable. In the third scenario, subsidence was set to a spatially uniform regional VLM, so the locally resolved case could be compared with a regional estimate and the no-subsidence case. This three-scenario approach enables a direct assessment of the extent to which subsidence, and its spatial resolution, alter coastal vulnerability patterns across the Volta Delta. All variables were ranked on a standardised scale before inclusion in the index to ensure comparability. Subsidence was treated as an independent parameter to capture its localised contribution to relative sea-level change, which may not be fully represented by regionally uniform sea-level rise estimates. The list of variables and their attributes is summarised in Table 1.



Figure 2. Methodology workflow for the three-scenario CVI assessment of the Volta Delta coastline, Ghana, using the square root of the product mean formula by Gornitz et al. [42]. $CVI_{+(v\text{-}sub)}$ uses the spatially resolved PS-InSAR subsidence as a ninth variable; $CVI_{+(u\text{-}sub)}$ uses a spatially uniform regional vertical land motion, and CVI_{-sub} excludes subsidence. All three indices are classified against a single combined quantile distribution to ensure direct comparability.

Coastal elevation, though included in some CVI formulations [42,43], was excluded from the vulnerability assessment for two reasons. First, the Volta Delta's uniformly low-lying terrain (the majority of the coastal fringes lie below the 2 m above mean sea level [40]) results in all grid cells being ranked as very high for elevation, hence failing to offer spatial variations. Second, in a subsiding delta, elevation and land subsidence are interrelated, with subsidence driving long-term elevation loss. Including both in the same index would create redundancy and obscure the effects of subsidence on coastal vulnerability, which is the study's primary focus.

Table 1. List of geological, geomorphological, hydrodynamic, and anthropogenic variables used for CVI computation, and their respective sources, resolutions and periods.

Parameters	Data Source	Resolution	Period
Subsidence/VLM	GNSS-validated InSAR-VLM [5]; NASA's IPCC Regional VLM, Tema gauge (PSMSL 1049), for the uniform subsidence scenario [44–46].	~20 m (InSAR); ~1° (regional VLM, applied uniformly)	2016–2020 (InSAR); 1995–2014 baseline (regional VLM)
Sea-Level Rise	NASA's IPCC Regional Sea Level Tool with data sourced from the IPCC Sixth Assessment Report (AR6), Working Group I [44–46].	1° × 1°	2020
Shoreline Change	Planet satellite imagery (https://www.planet.com/) and 2005 orthophotos (Geological Survey Authority (GSA)).	Planet = 4 m Orthophoto = 0.5 m	2005–2020
Coastal Slope	Global Coastal Characteristics Dataset [47,48].	1 km	2012–2023
Geology	GSA and BGR [49].	1:1,000,000	2009
Geomorphology	Planet satellite imagery, 2005 orthophotos (Geological Survey Dept.), and LULC maps [41].	Planet = 4 m Orthophoto = 0.5 m	2005–2020
Significant Wave Height	Global Atmospheric Reanalysis Interim data. Sources: ECMWF and Giardino et al. [50].	0.75°	2018
Mean Tidal Range	Tidal gauge data from GPHA (Tema) and MPS Terminal 3.	—	2016–2020
Land Use/Land Cover	Sentinel-2 land-cover time series [51].	10 m	2020

2.3.1. Uniform Regional or Spatially Resolved Local Subsidence Rates

Spatially resolved land subsidence rates for the Volta Delta were obtained from Avornyo et al.'s [5] study, which employed the Persistent Scatterer InSAR (PS-InSAR) technique. Sentinel-1 (S1) Single-Look Complex (SLC) SAR images with 250 km by 180 km Interferometric Wide (IW) swaths were used. The entire shore length of the study area was covered by two swaths (flight paths 147 and 74), both in ascending geometry. Each swath contained three sub-swaths, and three of the six sub-swaths together covered the full extent of the study area. For each of these three sub-swaths, 119 C-band (5.6 cm wavelength) images with vertical co-polarisation (VV) and ascending geometry were acquired from January 2016 to December 2020 (5 years). The PS-InSAR approach followed the SNAP-to-StaMPS chain [52], with a correction of residual atmospheric phase using the TRAIN toolbox by Bekaert et al. [53]. The analysis yielded 119,477 persistent scatterers at a density of 66.52 PS/km^2, with calibrated line-of-sight (LOS) velocities from 1.77 mm/yr (uplift) to −9.16 mm/yr (subsidence) and an overall mean of −3.25 mm/yr. Per-pixel displacement time series were extracted for each scatterer, with the twenty most-subsiding locations following a linear trend at an area-mean rate of -8.67 ± 0.27 mm/yr. Following Avornyo et al. [5], horizontal motion was assumed negligible, and the calibrated LOS velocities were interpreted as VLM. The InSAR-derived velocities were validated against a GNSS survey (precise point positioning) of seven Ground Control Points dotted along the coast, with the highest subsidence at Keta (−5.36 mm/yr) [5]. The surveyed control points were compared with the mean InSAR velocity within a 100 m radius of each. The mean absolute difference between the two datasets gave a calibration uncertainty of ±2.75 mm/yr. This single geometry assumption is a recognised limitation, and the ±2.75 mm/yr calibration margin against the vertical GNSS rates bounds the residual error, including any horizontal contribution. Full processing and validation details are provided by Avornyo et al. [5].

For the uniform subsidence scenario, the uniform regional VLM data were obtained from NASA's IPCC Regional VLM with data sourced from the closest tide gauge (Tema, PSMSL 1049) [44–46]. Both VLM sources were adopted for the two subsidence CVI scenarios and ranked based on the subsidence vulnerability classifications in Table 2. For the uniform regional VLM scenario ($CVI_{+(u\text{-}sub)}$), each grid cell was uniformly characterised with the regional VLM rate. In the case of the spatially resolved scenario ($CVI_{+(v\text{-}sub)}$), the mean VLM rate (mm/yr) in a grid cell was used to characterise that grid cell.

2.3.2. Sea-Level Rise

The regional or localised increase in sea levels is driven largely by climate forcings that translate into cascading hazards, which exacerbate coastal vulnerability. Due to the possibility of coastal land being inundated, coasts exposed to the rising sea level are considered highly vulnerable locations [54]. On the contrary, coasts with low rates of sea-level rise are relatively resilient and less susceptible to flooding [54]. In this study, a regional SLR change rate for 2020 was obtained from NASA's IPCC Regional Sea Level Tool with data sourced from the IPCC Sixth Assessment Report (AR6), Working Group I [44–46]. The 50th percentile of the Shared Socioeconomic Pathway (SSP) scenarios 2–4.5 and 5–8.5, characterised by moderate and very high greenhouse gas emissions, respectively, and without the IPCC VLM component, was selected. The VLM-free product was chosen to avoid double counting VLM, since subsidence is included in the CVI estimation separately. Due to spatial invariability at the selected extent, the SLR value of 4 mm/yr to 5 mm/yr (SSPs 2–4.5 and 5–8.5) was used to uniformly characterise each grid cell in the entire region.

2.3.3. Shoreline Change

Erosion and accretion rates indicate the dynamics of the coast and are used as proxy indicators for the potential impact of climate change. Unlike eroding coastlines, accreting coastlines are generally considered less vulnerable, since they contribute to coastline progradation that helps in incident wave energy dissipation. To obtain the rate of shoreline change, the shorelines of the 2005 orthophotos and 2020 Planet imagery were digitised and compiled in ArcGIS V. 10.7.1 into a single shapefile with relevant attributes. Using a manually delineated offshore baseline, the Digital Shoreline Analysis System (DSAS) tool, Version 5.1 of ArcGIS, was used to relatively estimate the changes between 2005 and 2020 following Jayson-Quashigah et al. [40]. To accurately quantify the variations along the beach, perpendicular transects were cast at 50 m intervals along the shore [55]. The End Point Rate (EPR) approach, used to assess and quantify the long-term movement and changes in coastal shorelines, was adopted for the assessment of the shoreline change rate. The EPR's key advantage lies in its computational simplicity and the minimal need for only two shoreline timestamps [56]. Shoreline change uncertainty was assessed by combining the positional uncertainties of the 2005 orthophotos and 2020 Planet imagery, yielding an estimated EPR uncertainty of ± 0.30 m/year. The mean shoreline change rate (m/yr) value in each grid was correspondingly ranked based on the shoreline change vulnerability classifications in Table 2.

2.3.4. Coastal Slope

The backshore slope, which is the sub-aerial profile from the shoreline to the first landward elevation peak, as defined by Athanasiou et al. [47], was used for the CVI estimation. The spatial distribution is a global dataset with transects spaced at 1 km, with each transect containing data sourced from both the Copernicus Digital Elevation Model (DEM) and the Delta Digital Terrain Model (DTM). Unlike the Copernicus DEM, which is a Digital Surface Model that includes buildings and vegetation canopy that may give false elevation peaks, the DeltaDTM—a Digital Terrain Model—was preferred for this study.

The coastal slope value (%) per grid, or the mean value for two or more slopes (transects) in a grid, was ranked based on the slope vulnerability classifications in Table 2.

2.3.5. Geology and Geomorphology

Erosivity risks, the potential for soil erosion, correlate with geology and coastal landform [57]. The erosion resistance of bedrock lithology, shore materials, and coastal landforms varies greatly [58]. Gornitz and Kanciruk [59] suggested a generalised scale of lithologic and geomorphologic resistance to erosion. The geological data were digitised from a 2009 1:1,000,000-scale geologic map by the Geological Survey Authority, Ghana (GSA) and Bundesanstalt für Geowissenschaften und Rohstoffe, Germany (BGR) [49]. In the case of geomorphology, data were sourced from a combination of 2005 orthophotos from the GSA, four-metre 2020 Planet satellite imagery, and a 2015 land-cover map obtained from Appeaning Addo et al. [41]. The dominant features for each variable (geology and geomorphology) in each grid were correspondingly ranked based on the geology and geomorphology vulnerability classifications in Table 2.

2.3.6. Significant Wave Height

Significant wave height (SWH) is a measure of the wave energy's ability to transport coastal sediment [57,60], and it greatly determines the morphodynamic regime of a coastline. Coastlines that have high wave heights are also known to be more vulnerable than those that are exposed to low wave heights [61]. SWH data were sourced from the global data provided by Giardino et al. [50] based on Global Atmospheric Reanalysis Interim data from the European Centre for Medium-Range Weather Forecasts (ECMWF) website (Table 1). The spatial variability along the coast of the study area was kept at 2 km intervals based on the grid cell positioning. The SWH value in each grid was ranked based on the SWH vulnerability classifications in Table 2. Where there was more than one dissimilar SWH value in a grid cell, the mean was used.

2.3.7. Mean Tidal Range

The mean tidal range has been used as a measure to assess coastal vulnerability in earlier research [57]. If a coastal location has a high tidal range, it is considered to be extremely susceptible because powerful tidal currents have an influence on coastal behaviour [42,62]. Thieler and Hammar-Klose [43] posited an opposite classification where microtidal coasts are rather the most vulnerable since the proximity of their coastlines to the high tide allows storm surges to easily overtop normal water levels, hence causing immediate flooding. The classification by Thieler and Hammar-Klose [43] was adopted for this study. Daily tidal data were obtained from the Ghana Ports and Harbours Authority, as well as the Meridian Port Services Terminal 3, the closest tide station to the study area, from 2016 to 2020. The mean tidal range (m) was then estimated from the dataset and used to uniformly characterise each grid cell.

2.3.8. Land Use and Land Cover (LULC)

Land-cover and land-use patterns are human-driven and essentially complement the physical or environmental component [63] of CVI estimation. LULC is incorporated as an anthropogenic exposure dimension rather than as a measure of physical susceptibility. Some land-use patterns can cause severe repercussions on landforms, thus exacerbating the prevalent deteriorating conditions. The land-cover maps for the study area were obtained from global data provided by Karra et al. [51] using Sentinel-2 images (10 m resolution) and a machine learning algorithm. The dominant land cover in each grid was ranked based on the LULC vulnerability classifications in Table 2.

2.4. Coastline Segmentation and Grid Cell Design

In the second stage of the methodology, approximately 150 km of the Volta Delta coastline was divided into 72 contiguous grid cells (Figure 1), each spanning 2 km alongshore. The 2 km by 2 km grid was selected for a balanced spatial resolution that is sufficient to detect meaningful variation across the nine (9) input variables and ensure an even grading of the input data, with each cell receiving input from all variables. A grid-resolution sensitivity test (Supplementary Material S1) supports this choice. At 2 km, every coastal cell receives all nine variables, whereas at 1 km and 0.5 km, 22% and about 66% of the cells fall between the sampling points of the coarser inputs, respectively, and cannot be fully scored. Each variable was assigned to a cell by a method matched to its native resolution (Table 1). The mean value or dominant class was used to characterise grid cells of variables with fine resolution, whereas single data points were sampled for some coarse gridded variables, with sea level and tidal range applied uniformly. No variable was upsampled beyond its source resolution (Supplementary Table S1). All spatial data were projected in WGS 1984 UTM Zone 31N (EPSG: 32631) to ensure metric consistency across datasets.

2.5. Coastal Vulnerability Index Computation

The third stage of the methodology involved the quantification and ranking of each variable within each of the contiguous grid cells. The variables are quantified and categorised based on a standardised scale of one to five [55,57,58,60], with the magnitude of vulnerability increasing from one (1 = very low vulnerability) to five (5 = very high vulnerability). In each of the seventy-two (72) 2 km by 2 km grid cells, each of the nine (9) variables is categorised individually based on the 1-to-5 vulnerability scale (Table 2). Within each grid cell, the mean value of continuous variables (shoreline change, nearshore slope, subsidence, SLR, significant wave height, and mean tidal range) was computed as the representative cell value. For categorical variables (geology, geomorphology, and land cover), the dominant class within each cell was assigned as the representative value.

Table 2. Quantification and ranking of selected variables based on the 1-to-5 vulnerability scale, with the vulnerability rank ranging from one (1 = very low vulnerability) to five (5 = very high vulnerability).

Parameters	Very Low (1)	Low (2)	Moderate (3)	High (4)	Very High (5)
Subsidence (mm/yr) [57]	>1.0 Uplifting	1.0–−1.0	−1.0–−2.0	−2.0–−4.0	<−4.0 Subsiding
Sea-Level Rise (mm/yr) [61]	<0.8	0.8–1.6	1.6–2.4	2.4–3.2	>3.2
Shoreline Change (m/yr) [57]	>2.0 Accretion	1.0–2.0	−1.0–1.0	−1.0–−2.0	<−2.0 Erosion
Coastal Slope (%) [64]	>12	8–12	4–8	2–4	<2
Geology [57]	Plutonic volcanic (lava) high-medium grade metamorphics	Low-grade metamorphics, sandstone and conglomerate (well-cemented)	Most sedimentary	Coarse and/or poorly sorted unconsolidated sediments	Fine unconsolidated sediment volcanic ash
Geomorphology [57]	Rocky, cliffed coast, fjords, fiards	Medium cliffs, indented coasts	Low cliffs, glacial drift, salt marsh, coral reefs, mangrove	Beaches (pebbles), estuaries, lagoons, alluvial plains	Barrier beaches, beaches (sand), mud flats, deltas
Significant Wave Height (m) [65]	<0.55	0.55–0.85	0.85–1.05	1.05–1.25	>1.25
Mean Tidal Range (m) [43]	>6.0 Macrotidal	4.0–6.0	2.0–4.0 Mesotidal	1.0–2.0	<1.0 Microtidal
Land Use/Land Cover [66]	Water bodies, marsh/bog and moor, sparsely vegetated areas, bare rocks	Natural grasslands, coastal areas	Forest	Agriculture	Urban and industrial infrastructure

Gornitz [42,67] established one of the foremost methods for computing the overall CVI by dividing the square root of the product of ranked variables by the total number of variables. The index is a relative physical coastal vulnerability, or susceptibility, index; it does not incorporate adaptive capacity and is therefore not a full risk assessment. The variables used in computing the overall CVI were unweighted, following Gornitz [42], Thieler and Hammar-Klose [60], and Boateng et al. [29]. The unweighted formulation was retained to maintain comparability with prior assessments along the Ghanaian coast [17,29] and to isolate the specific contribution of subsidence inclusion from any effects of variable weighting. The implications of this assumption are addressed in the limitations section.

The CVI computation stage (fourth stage) integrates all variables into a single composite index by adopting the square root of the product mean formula established by Gornitz [42]. To assess the magnitude of impact subsidence could have on the vulnerability of the coastal zone to hazards, three CVIs were calculated: the spatially variable InSAR-derived land subsidence ($CVI_{+(v\text{-}sub)}$, Equation (1)); the spatially uniform subsidence set to the regional VLM ($CVI_{+(u\text{-}sub)}$, Equation (1)); and the CVI without subsidence ($CVI_{\text{-}sub}$, Equation (2)).

$$CVI_{+(v\text{-}sub)\ OR+(u\text{-}sub)} = \sqrt{\frac{SC \times GL \times S \times CS \times GM \times MTR \times SLR \times LULC \times SWH}{9}} \quad (1)$$

$$CVI_{(\text{-}sub)} = \sqrt{\frac{SC \times GL \times CS \times GM \times MTR \times SLR \times LULC \times SWH}{8}} \quad (2)$$

where $CVI_{+(v\text{-}sub)}$ = CVI with spatially resolved subsidence; $CVI_{+(u\text{-}sub)}$ = CVI with the regional uniform subsidence; $CVI_{\text{-}sub}$ = CVI without subsidence; SC = shoreline change; GL = geology; S = subsidence; CS = coastal slope; GM = geomorphology; MTR = mean tidal range; SLR = sea-level rise; LULC = land use/land cover; and SWH = significant wave height.

In stage five, the CVI values from $CVI_{+(v\text{-}sub)}$, $CVI_{+(u\text{-}sub)}$, and $CVI_{\text{-}sub}$ were combined into one single dataset, and the vulnerability classes were derived from the combined distribution by splitting the dataset into four quantile ranges. The quantile thresholds were applied consistently across the three CVI scenarios to ensure direct comparison between them. The vulnerability classes were: 0% to 25% (22–73) = low vulnerability; 25% to 50% (73–103) = moderate vulnerability; 50% to 75% (103–147) = high vulnerability; and 75% to 100% (147–333) = very high vulnerability.

Finally, using a quantitative measure of the impact land subsidence has on coastal vulnerability, the following equation (Equation (3)), which computes the relative change in CVI, was used to quantify the compounding influence of land subsidence on coastal vulnerability for each grid and to identify the most vulnerable hotspots along the Volta Delta coast. The relative change estimation is an indication of the percentage increase or decrease in CVI for each grid cell pair.

$$\%\Delta CVI = \frac{CVI_{(A)} - CVI_{(B)}}{CVI_{(B)}} \times 100 \quad (3)$$

For each grid cell pair, $CVI_{(A)}$ = the grid with the higher CVI values and $CVI_{(B)}$ = the grid with the lower CVI values.

The result of the relative change in CVI between each CVI pair and for each grid was classified into increase or decrease categories. Between each pair of the three scenarios, the corresponding transitions between vulnerability classes for each grid were also identified using categorical classifications as follows: vulnerability class decrease; no change in vulnerability class; and vulnerability class increase (+1 increase, +2 increase, +3 increase,

and +4 increase). In complementing the relative change estimation and vulnerability-class transition map, a Wilcoxon signed-rank test was applied to summarise the direction and consistency of the paired CVI differences between each pair of scenarios. Because the ranking and multiplicative index structure make a higher score expected once a subsidence rank is added, the test is treated as a descriptive comparison rather than independent confirmation of a physical effect. The Wilcoxon signed-rank test, a non-parametric test, was selected because of the composite nature of the CVI values, which involved the ranking and multiplication of variables and may not truly be normally distributed, even if normality tests portray this as such.

All the processing steps described above are implemented in the dynamic, automated CVI assessment tool, which is a configuration-driven, interactive Python (v3.10.4) pipeline that turns GIS variables into vulnerability maps, ranks, and statistics. The code and its documentation are available on GitHub (see Data Availability Statement).

3. Results

3.1. Geological, Geomorphological, Hydrodynamic, and Anthropogenic Variables for CVI

Figure 3a–i display maps of the input data from the various sources used in this study. The maps indicate the range and gradation of values for continuous variables or the various classes in the case of categorical variables, obtained from the corresponding variable sources.

Figure 4 shows the vulnerability-ranked maps of each of the nine (9) variables used in computing the CVI for the Volta Delta. For each variable, it gives a breakdown of the varied vulnerability classification of the delta's entire coast using the corresponding vulnerability (colour) classification scheme shown in Table 2.

3.1.1. Subsidence and Sea-Level Rise

Figure 3a shows the rate of subsidence along the coast in mm/yr, with values ranging from -2.44 mm/yr to -4.23 mm/yr and an average value of -3.35 mm/yr. Using the mean subsidence rates in each grid cell, 87.5% of the shoreline indicated high vulnerability, whereas the remaining 12.5% of the coast showed very high vulnerability. The spatially uniform regional VLM was about -0.1 mm/yr. Figure 3b shows the spatially uniform rate of SLR (mm/yr) along the delta's coast. The entire coastline of the delta is experiencing SLR of 4 mm/yr–5 mm/yr, thus indicating a very high vulnerability status.

3.1.2. Shoreline Change

Figure 3c shows the rate of shoreline change (m/yr) along the delta's coast, ranging from an eroding coast (-12.02 m/yr $\pm$ 0.30) to an accreting coast (7.30 m/yr $\pm$ 0.30), with a net average of -0.66 m/yr $\pm$ 0.30 (erosion). Using the mean shoreline change value per grid cell, 6.94% of the shoreline showed very low vulnerability; 4.17% of the shoreline showed low vulnerability; 51.39% of the shoreline showed moderate vulnerability; 22.22% of the shoreline showed high vulnerability; and 15.28% showed very high vulnerability.

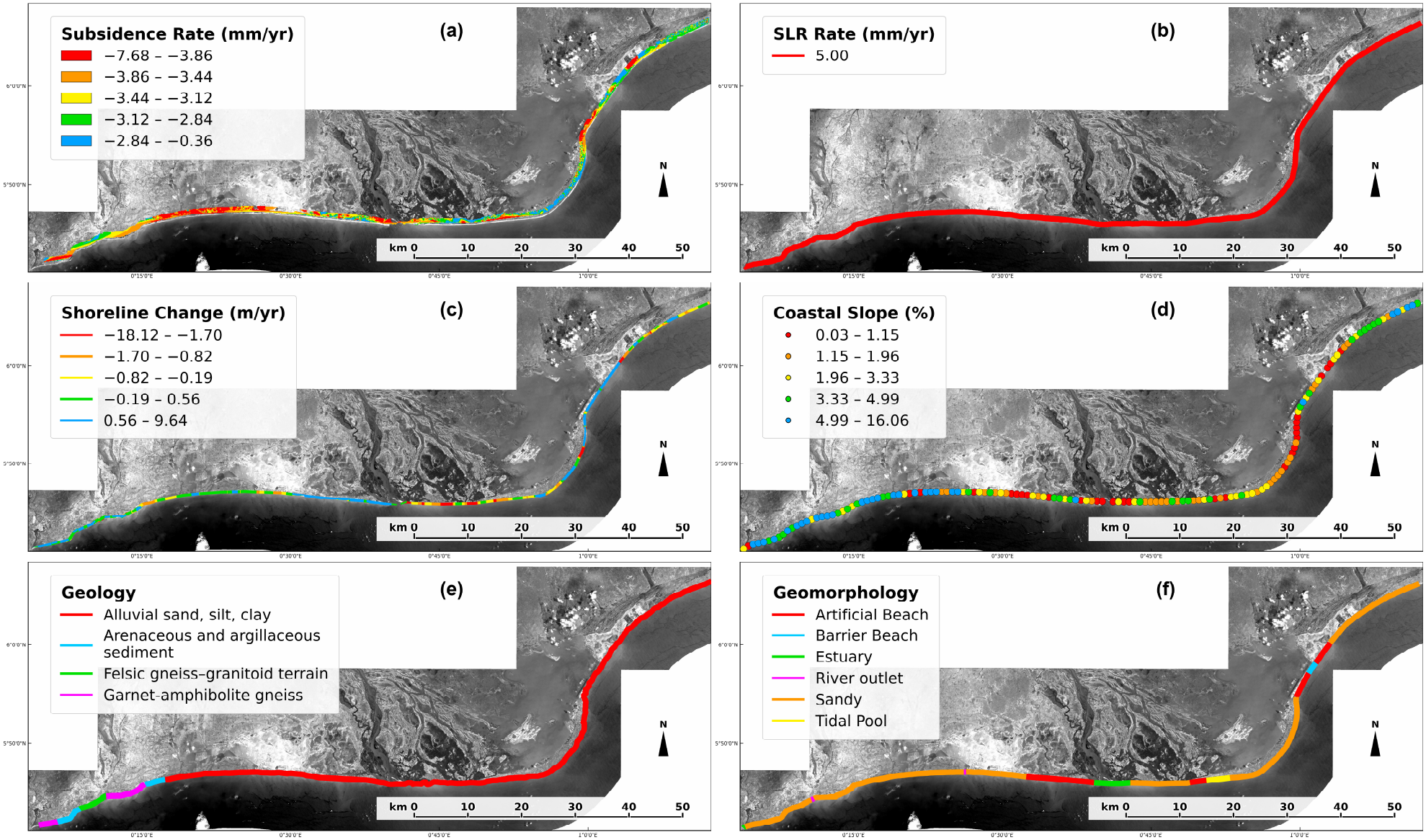


Figure 3. *Cont.*

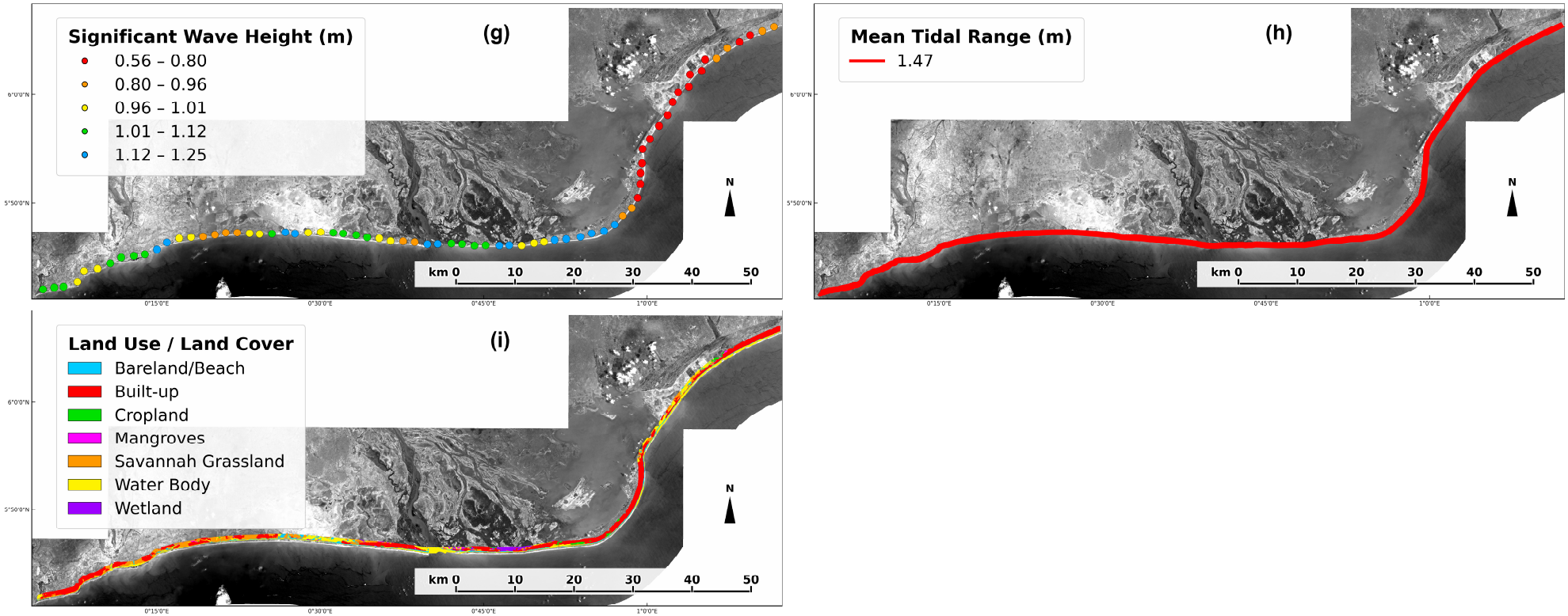


Figure 3. Maps showing CVI input parameters (continuous values and categorical classes) for: (**a**) subsidence, (**b**) sea-level rise, (**c**) shoreline change, (**d**) coastal slope, (**e**) geology, (**f**) geomorphology, (**g**) significant wave height, (**h**) mean tidal range, and (**i**) land use/land cover.

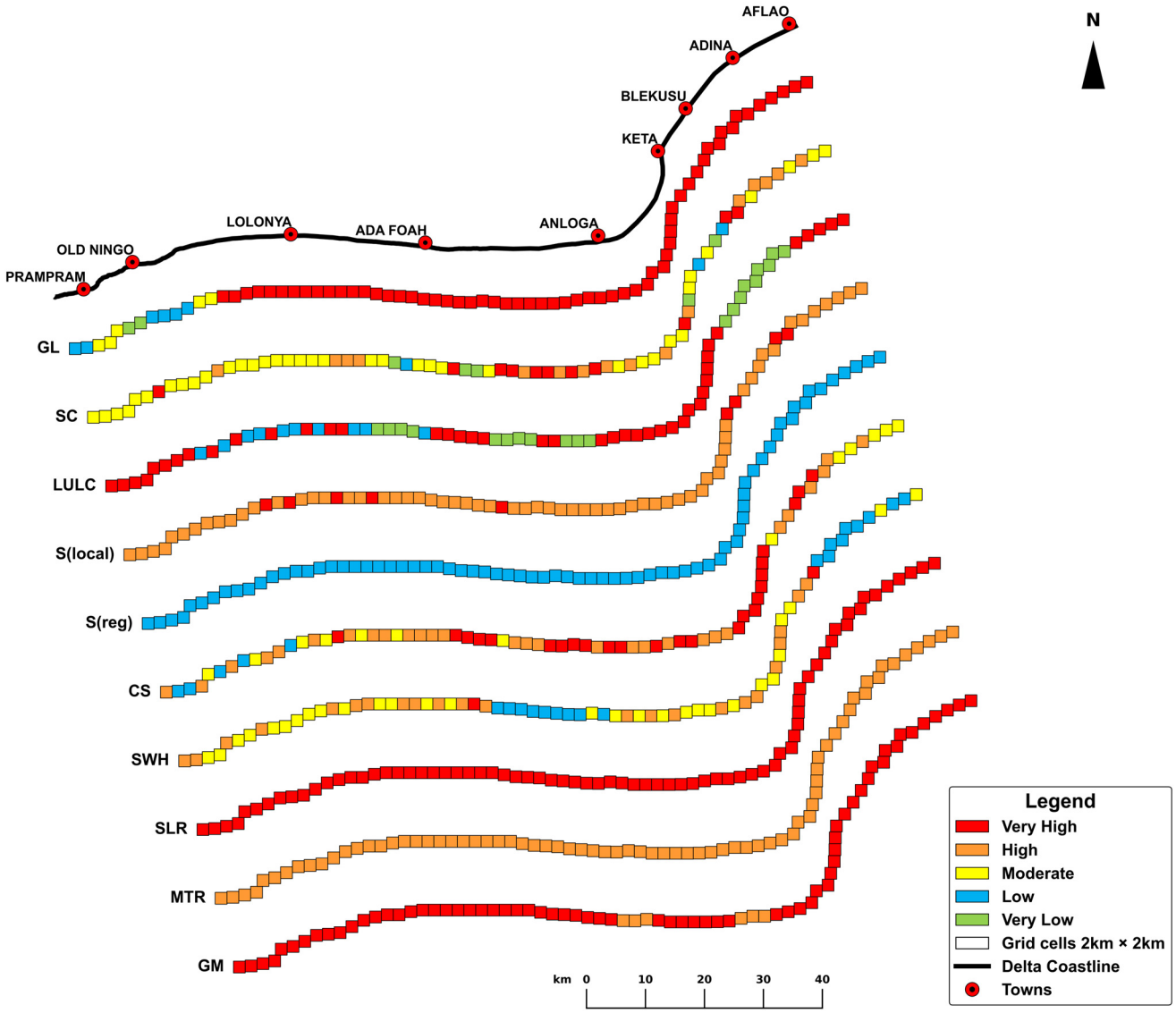


Figure 4. A map showing the quantification and ranking of selected variables based on the one-to-five vulnerability scale, with the vulnerability rank ranging from one (1 = very low vulnerability) to five (5 = very high vulnerability). The variables are SC = shoreline change; GL = geology; S(local) = local subsidence; S(reg) = regional subsidence; CS = coastal slope; GM = geomorphology; MTR = mean tidal range; SLR = sea-level rise; LULC = land use/land cover; and SWH = significant wave height.

3.1.3. Coastal Slope, Geology, and Geomorphology

Figure 3d shows the coastal slope (%) of the coast ranging from 0.18% to 11.04%, with an average of 3.28%. Using the mean coastal slope value in each grid cell, 6.94% of the shoreline showed low vulnerability; 18.06% of the shoreline showed moderate vulnerability; 40.28% of the shoreline showed high vulnerability; and 34.72% showed very high vulnerability. Figure 3e shows the geology classes along the coast, with the "unconsolidated alluvial sand, silt and clay" class being the most extensive class. Using the most dominant geology class in each grid cell, 2.78% of the shoreline indicated very low vulnerability; 8.33% of the shoreline showed low vulnerability; 6.94% of the shoreline showed moderate vulnerability; and the remaining majority of 81.94% indicated very high vulnerability. Figure 3f shows the geomorphology classes along the coast, with the most dominant class being the "beaches (sand) or barrier beaches" class. Using the most dominant geomorphology class in each grid cell, 8.33% of the shoreline indicated high

vulnerability, whereas the remaining majority of 91.67% indicated coasts with very high vulnerability status.

3.1.4. Significant Wave Height and Mean Tidal Range

The highest significant wave height (m) obtained was 1.25 m, whilst the lowest was 0.56 m (Figure 3g), with an average of 0.95 m. Using the mean significant wave height value in each grid cell, 25% of the shoreline indicated low vulnerability; 40.28% of the shoreline showed moderate vulnerability; 31.94% of the shoreline indicated high vulnerability; and 2.78% indicated very high vulnerability. Figure 3h shows the mean tidal range (m) along the coast. The entire coastline of the delta is experiencing a spatially uniform mean tidal range of 1.47 m, thus indicating a high vulnerability status.

3.1.5. LULC

Figure 3i shows the LULC classes along the delta's coast, with the most dominant class across the entire coast being built-up areas (urban and industrial infrastructure). Using the most dominant land cover in each grid cell, 27.78% of the shoreline showed very low vulnerability; 13.89% of the shoreline indicated low vulnerability; and the remaining 58.33% showed very high vulnerability.

The percentage distribution of grid cell ranking, based on the 1–5 vulnerability scale for each variable, is summarised in Table 3. Individually, six out of the nine variables had more than 50% of the coastline indicating high (two variables) to very high (four variables) vulnerability.

Table 3. Percentage distribution of vulnerability ranks per variable.

Variables	Very High (%)	High (%)	Moderate (%)	Low (%)	Very Low (%)
Local Subsidence (spatially resolved) *	12.50	87.50	—	—	—
Regional Subsidence (uniform)				100	
Sea-Level Rise **	100	—	—	—	—
Shoreline Change	15.28	22.22	51.39	4.17	6.94
Coastal Slope	34.72	40.28	18.06	6.94	—
Geology **	81.94	—	6.94	8.33	2.78
Geomorphology **	91.67	8.33	—	—	—
Sig. Wave Height	2.78	31.94	40.28	25	—
Mean Tidal Range *	—	100	—	—	—
LULC **	58.33	—	—	13.89	27.78

** Variable that indicated very high vulnerability for >50% of the coastline. * Variable that indicated high vulnerability for >50% of the coastline. Each header row colour corresponds with the colour code used for the various vulnerability ranks.

3.2. Comparing the Estimated Composite CVIs and Identifying Hotspots

The composite CVI for each of the seventy-two (72) grid cells, under the three scenarios are shown in Figure 5B. Without subsidence, CVI_{-sub} ranged from 22 to 177, with a mean CVI of 82 (moderate vulnerability). With the spatially resolved local InSAR subsidence, $CVI_{+(v\text{-}sub)}$ ranged from 42 to 333, with a mean CVI of 156 (very high vulnerability). The regional estimate scenario $CVI_{+(u\text{-}sub)}$, which uses the same nine variables but a spatially uniform subsidence set to the IPCC AR6 regional rate, ranged from 30 to 236, with a mean of 109 (high), intermediate between the other two. The grid cells with the highest CVI estimation across all three scenarios were grid cells 39 and 56, whereas the grid cell with the lowest CVI estimation was grid cell 34. Because the composite index is multiplicative, the change in the mean is not interpreted directly; the shifts in vulnerability class and in the

alongshore pattern are reported below. Classified against the common quantile thresholds (the horizontal reference lines in Figure 5B), the three scenarios produced distinctly different vulnerability classes for many cells (Figure 5A).

(A)

Composite CVI Ranking	CVI+(v-sub)	CVI+(u-sub)	CVI-sub
Very High	34	16	4
High	20	16	16
Moderate	11	20	19
Low	7	20	33

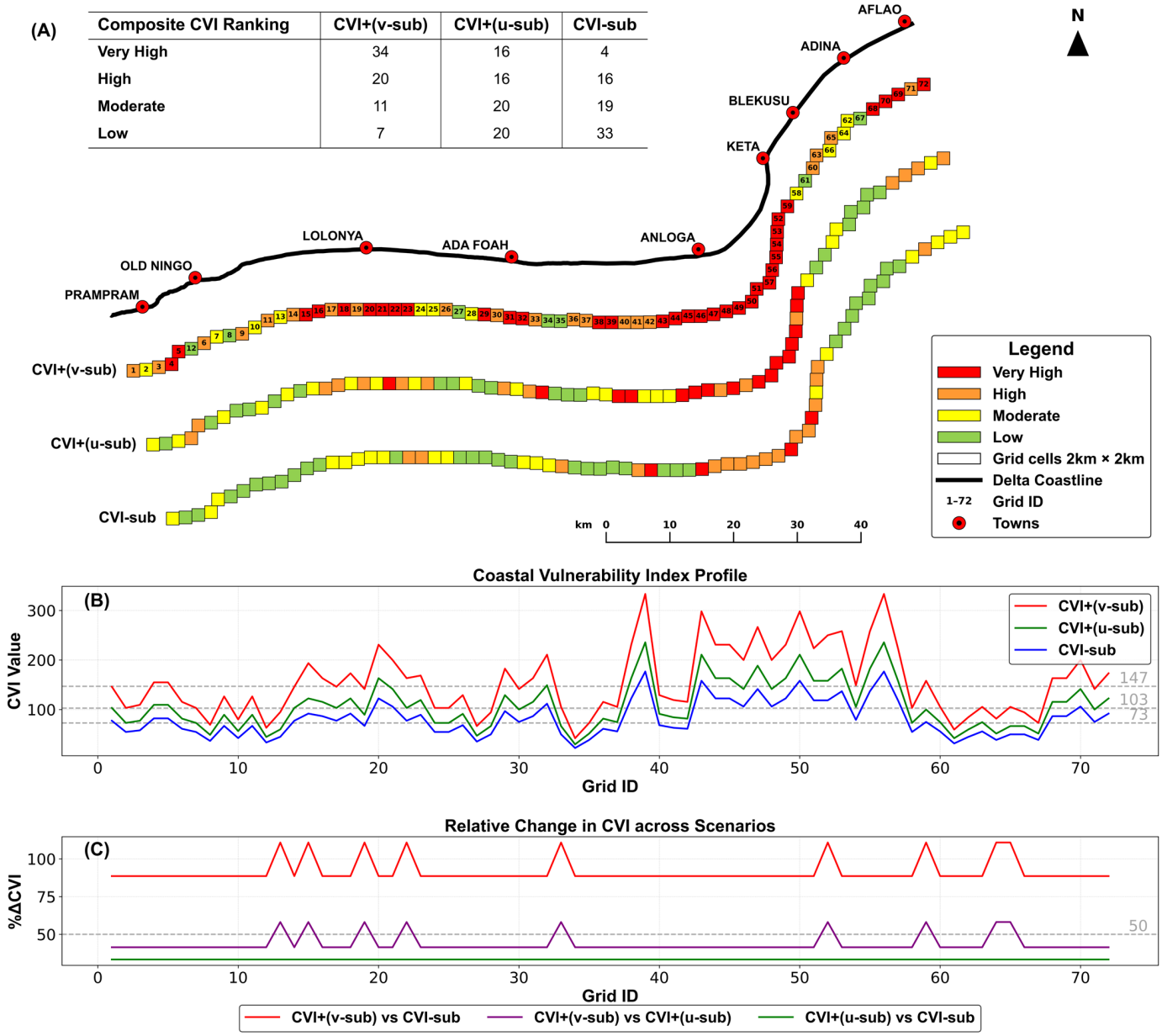


Figure 5. (**A**) A map showing the composite CVI rankings of the three scenarios per grid, $CVI_{+(v\text{-}sub)}$, $CVI_{+(u\text{-}sub)}$, and $CVI_{\text{-}sub}$, based on the vulnerability rank, which ranged from low vulnerability to very high vulnerability. (**B**) A line plot showing the composite CVI estimations per grid cell for the three scenarios and the quantile thresholds represented by the horizontal references for categorising the composite CVI ranking. (**C**) A line plot showing the relative change in CVI per grid between each pair of the three scenarios. All relative changes in CVI values (%) per grid are a step function set by the subsidence rank and are not interpreted as a magnitude of vulnerability change.

Complementing the grid cell map, the table in Figure 5A gives a count breakdown for vulnerability ranks across the three scenarios. Under $CVI_{+(v\text{-}sub)}$, seven (9.7%) cells were low, 11 (15.3%) were moderate, 20 (27.8%) were high, and 34 (47.2%) were very high; under $CVI_{+(u\text{-}sub)}$, 20 (27.8%) were low, 20 (27.8%) were moderate, 16 (22.2%) were high, and 16 (22.2%) were very high; and under $CVI_{\text{-}sub}$, 33 (45.8%) were low, 19 (26.4%) were moderate, 16 (22.2%) were high, and four (5.6%) were very high. The share of cells in

the high or very high classes rose from 28% (20 cells) with no subsidence, through 44% (32 cells) with the regional estimate, to 75% (54 cells) with the local InSAR. Across all three scenarios, the alongshore profile is similar (Figure 5B), peaking along the Keta and Songor lagoon margins (Figure 1), which hold most of the very high cells (Figure 5A); the rank correlations and hotspot-membership statistics confirming this stability are given in the Supplementary Materials (S2). The relative change in CVI (Figure 5C) is a step function set by the subsidence rank; therefore, because the index is multiplicative, the comparison rests on the vulnerability-class transitions (Figure 6) and the three-scenario class distribution rather than on the relative-change magnitude.

ΔVul Rank (Transition)	+(v-sub) vs -sub	+(v-sub) vs +(u-sub)	+(u-sub) vs -sub
Vulnerability Increase (+2)	29	4	0
Vulnerability Increase (+1)	32	45	37
No Change	11	23	35

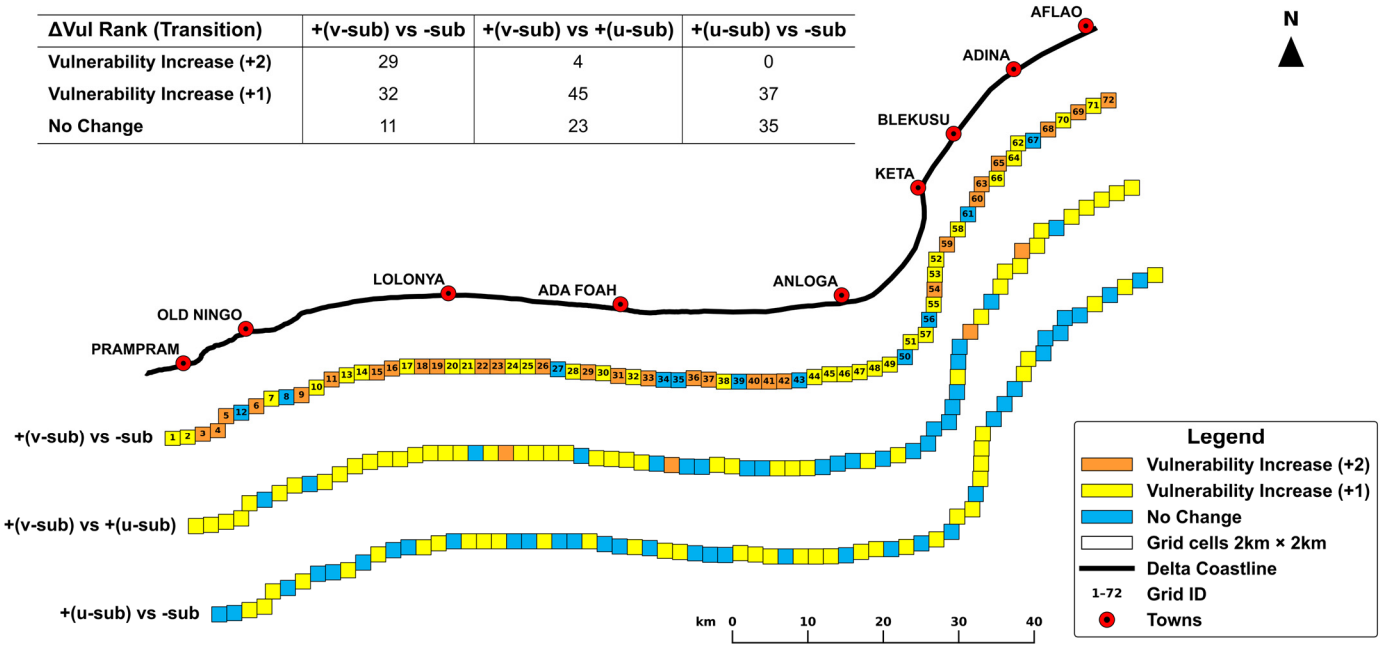


Figure 6. A map showing the vulnerability-class transitions between each pair of the three scenarios. Each strip corresponds to one pair of scenarios.

3.3. Vulnerability Rank Transitions

Figure 6 shows the vulnerability-class transitions for each pair of the three scenarios; the largest changes are between $CVI_{+(v\text{-}sub)}$ and $CVI_{\text{-}sub}$. Using the transition categories for each grid-pair transition between $CVI_{+(v\text{-}sub)}$ and $CVI_{\text{-}sub}$, 11 (15.3%) of the grid cells maintained their vulnerability rank status between $CVI_{+(v\text{-}sub)}$ and $CVI_{\text{-}sub}$; 32 (44.4%) of the grid cells transitioned one level up on the vulnerability scale from a lower vulnerability scale ($CVI_{\text{-}sub}$) to a higher vulnerability scale ($CVI_{+(v\text{-}sub)}$); and 29 (40.3%) of the grid cells transitioned two levels up the vulnerability scale from a lower vulnerability scale ($CVI_{\text{-}sub}$) to a higher vulnerability scale ($CVI_{+(v\text{-}sub)}$). Similar trends are shown by the other grid-paired transitions (Figure 6). No decrease in vulnerability status was recorded. Across all 72 paired grid cells, the CVI was higher when subsidence was incorporated, with a uniformly positive difference summarised by the Wilcoxon signed-rank test ($W = 0.00$, $n = 72$, $p < 0.001$). This follows from the ranking and multiplicative structure of the index and is reported as a descriptive comparison rather than independent statistical confirmation of the physical effect of subsidence. The robustness of these transitions to the InSAR subsidence uncertainty is confirmed by the Monte Carlo analysis (Supplementary Materials, S3).

4. Discussion

4.1. Comparing the Computed CVIs

All variables included in computing the CVIs tend to exacerbate the vulnerability of a coastal zone and the socio-economic livelihood therein, especially when individual rates or magnitudes exceed normal thresholds. Gornitz [42] and Thieler and Hammar-Klose [43] identified six or seven of the variables as the most crucial components in coastal vulnerability assessment, namely geomorphology, geology, coastal slope, relative SLR (eustatic and isostatic SLR), shoreline change, mean tidal range, and mean wave height, while land use or land cover was included to capture the anthropogenic dimensions of exposure. Along the coast of Ghana, the only CVI assessments that incorporate land subsidence were carried out on a regional (Greater Accra Region) scale by Appeaning Addo [17] and extensively along the entire coast of Ghana on a district scale by Boateng et al. [29]. In both instances, data on all variables except subsidence were either measured directly or sourced as secondary data from reliable institutions. Both studies by Appeaning Addo [17] and Boateng et al. [29] assumed average and spatially invariant subsidence rates of -2 mm/yr and ≤ -1 mm/yr, respectively, based on global trends and tide gauge data. The present study is therefore the first CVI assessment along the coast of Ghana to incorporate GNSS-validated, InSAR-derived subsidence rates in the overall CVI computation. To assess the differences in vulnerability attributable to subsidence, a comparative approach was adopted, computing three indices spanning no subsidence (CVI_{-sub}), a spatially uniform regional estimate ($CVI_{+(u\text{-}sub)}$), and the spatially resolved InSAR subsidence ($CVI_{+(v\text{-}sub)}$).

The three-scenario computation demonstrates that incorporating measured, spatially resolved subsidence alters the vulnerability profile of the delta's coastline (Figure 5B). The mean composite CVI increased from 82 for CVI_{-sub}, a moderate vulnerability status, to 156 for $CVI_{+(v\text{-}sub)}$, a very high vulnerability status, with the regional estimate scenario intermediate at 109; because the index is multiplicative, these magnitudes are not interpreted directly. Along with the mean-related increase in the vulnerability status was a shift in the classification structure for the individual grid cells: 75% of the grid cells indicated high or very high vulnerability under $CVI_{+(v\text{-}sub)}$, compared with the majority (72%) indicating moderate to lower vulnerability under CVI_{-sub}. The vulnerability rank transitions also reinforce the pattern: 84.7% of the grid cells (61 of 72) moved at least one class upward when spatially resolved subsidence was incorporated, while 40.3% (29) moved two classes upward, with no cell indicating a decrease in vulnerability. The other vulnerability rank transition pairs, summarised in Figure 6, emphasise the pattern. The regional VLM estimate would, by contrast, place only 44% of the coast in the high or very high classes, so the locally resolved InSAR recovers a severity of vulnerability that a regional value misses. Given that the compared indices are derived from the same 72 contiguous grid cells and share the same variables except subsidence, the paired differences are consistently positive across all cells (Wilcoxon signed-rank test, $p < 0.001$), which should be interpreted as a descriptive comparison rather than an independent confirmation of the physical effect of subsidence. The composite CVI values per grid cell, the classification transitions and the paired test all point to the same conclusion that excluding land subsidence from CVI computation understates the vulnerability of the delta's coast.

Land subsidence directly amplifies the local rate of SLR and its cascading impacts. The grid cell subsidence inputs, ranging from -2.44 to -4.23 mm/yr (mean of -3.35 mm/yr), are therefore of almost the same magnitude as the regional SLR rates of 4 to 5 mm/yr. This translates into the compounding effect of land subsidence on SLR rates, suggesting an amplification of the impacts of eustatic SLR by almost a twofold factor. This doubling effect is inapparent to assessments that rely on globally averaged or assumed subsidence, as applied by the uniform regional VLM in this study and the only CVI studies [17,29] along

Ghana's coast that incorporated land subsidence. While the grid cell means of the PS-InSAR data smooth out localised extremes, the highest point-scale subsidence rate recorded was 7.68 mm/yr (Figure 3a), which far exceeds the regional SLR rates of 4 to 5 mm/yr. This is consistent with global evidence that VLM frequently rivals or exceeds eustatic SLR as the dominant driver of relative sea-level change in deltas [5,7,8].

On the standardised 1–5 vulnerability scale adopted for this study, the averaged spatially resolved subsidence rates place 87.5% of the grid cells in high subsidence class and the remainder in the very high class (Table 3), whereas the estimations used by the previous studies (e.g., Boateng et al. [29]) would have understated the compounding effect of subsidence by ranking the vulnerability status of the grid cells two or three classes lower, thus moderate to low status. A comparable dual-scenario CVI assessment by Husnayaen et al. [55] in Semarang, Indonesia, similarly reported obvious reclassification of grid cells when measured land subsidence rates were used, suggesting that the pattern observed is characteristic of subsiding deltaic coasts and not peculiar to the Volta Delta. Higher subsidence rates would translate into a higher subsidence vulnerability rank and hence exacerbate the magnitude and frequency of prevalent coastal multi-hazards such as flooding and complete inundation, coastal erosion, saltwater intrusion, and loss of wetlands and ecosystem services.

4.2. Vulnerability Hotspots, Low-Risk Zones, and the Driving Variables

The high overall quantile or percentile distribution used in ranking each of the grid cells across the three scenarios was due largely to the high vulnerability status of the individual variables. Seven out of the nine variables had major sections (>58–100%) of the delta's coastline registering either very high or high vulnerability status (Table 3). The largest contributors were sea-level rise, geomorphology, geology, and LULC, with 100%, 91.67%, 81.94%, and 58.33% of the coastline, respectively, registering very high vulnerability. Most of these high contributors were not spatially variant.

In terms of vulnerability hotspots, all three scenarios displayed similar alongshore profiles and peaked at the coastal margins of the dominant Keta and Songor lagoons (Figure 5B); however, peaks along the Keta lagoon's coastal margin showed relatively higher values when compared with Songor lagoon's coastal margin. The grid cell with the lowest vulnerability under all three scenarios is grid cell 34. Grid cell 34 is located at the mouth or estuarine area of the Volta River, and owing to its location, it recorded the lowest rank for the following reasons. It has a very low vulnerability rank under the LULC variable due to the dominance of the low-ranked water body class, and a very low vulnerability rank under the shoreline change variable since the dominance of water means there is little to no shore to erode. It also has a patch of alluvial beach reinforced with groynes, which has drastically reduced erosion (very low vulnerability rank) and widened the beach. The cell also has a low vulnerability rank under SWH due to submerged fluvial deposit shoals at the river mouth that dissipate wave energy approaching the grid cell's coast. Despite a low coastal slope (very high rank) to aid the river's directional flow into the sea, and pockets of subsiding islands in the landward extent of the grid cell, the influence of the aforementioned low-ranked variables outweighed the high-ranked variables. On the contrary, the grid cells that recorded the highest composite values under all three scenarios were grid cells 39 and 56, which are dotted along the Keta lagoon's coastal margin, reaffirming the Keta coastal margin's relatively higher vulnerability status. Except for MTR, subsidence (case of $CVI_{+(v\text{-}sub)}$) and SWH, which indicated a high rank, all other variables showed a very high rank. These hotspots are stable to the choice of cell size. Across the grid resolutions that the input data adequately support, the Songor margin

stays within the top decile of vulnerability, and the Keta hotspot is most distinct at the 2 km resolution (Supplementary Material S1, Figure S1a).

Focussing on the composite $CVI_{+(v\text{-}sub)}$, the 54 grid cells that indicated high or very high composite vulnerability (Figure 5A) concentrate along the Keta lagoon margin (cells 36 to 57 and 59), the Songor lagoon margin (cells 14 to 23, 26 and 29 to 33), the Easternmost Denu–Aflao coast (grid cells 68 to 72), and smaller clusters along the Blekusu–Agavedzi stretch and the western delta. These hotspots are robust to the InSAR subsidence uncertainty, as shown by a Monte Carlo propagation reported in the Supplementary Materials (S3). These spatial distribution trends highlight a number of driving factors. For geology, 70% of the entire delta is predominantly covered by erodible alluvial deposits of sand, silt and clay [5], with gentle slope gradients that make it extremely vulnerable to SLR or storm surge, while the sandy barrier beach geomorphology compounds the vulnerability. These depositional landforms offer little inherent resistance to erosive and inundation forces. The little to no inherent resistance of the depositional landforms is heightened along the delta's coast by the long-standing reduction in fluvial sediment supply following the construction of the Akosombo dam [68,69]. Additionally, the coast of both lagoons has relatively thin barrier beaches (beach width), especially in the Songor area and Keta to Hlorve township, with pockets of extensive shoreline erosion. This is corroborated by the extensive revetments and groynes constructed at Ada, Dzita, Keta, Ningo–Prampram, and recently at Blekusu–Agavedzi to prevent further erosion. In the case of Keta, Kumapley [39] reported a 1000 m shoreline recession since 1880, while Fiadzigbey [70] indicated that about 70% of the town is now submerged underwater. The land-cover or land-use patterns along the Agorkedzi–Keta stretch are dominated by built-up areas and extensive agricultural farmlands, which increase the composite CVI, coupling physical exposure to socio-economic exposure.

These lagoonal margins additionally face constrained adaptation space. Bounded by the sea on one side and the lagoon water bodies on the other (Figure 7a), the barrier coastlines lack natural landward retreat pathways. Given this setting, the sand barrier is predicted to experience coastal narrowing as defined by Pontee [71], that is, a reduction in the coastal width, due to increased water levels at both the seaward boundary from SLR and the landward boundary (Figure 7a) from inland flooding of the Volta River or from rising lagoon levels driven by the inland influx of seawater. In locations protected by groynes or revetments, such as Keta and Dzita, the rate of coastal squeeze will increase. The presence of these structures only stabilises the local shoreline while displacing erosion downdrift [38], as shown by eroded coastline images along the Blekusu–Agavedzi stretch (Figure 7b–d), downdrift of the Keta Sea Defence Project. The presence of defence structures also prevents the landward migration of ecosystems, leading to the loss of unique coastal habitats and ecosystems (e.g., Doody [72]). Inundation of the coast from the seaward boundary will also push the salt wedge further up into freshwater aquifer systems, with consequences for agricultural activities, livelihoods and human health. Cases of saltwater intrusion are already reported along the coast [73], particularly in the towns dotted along the Bight of Benin.

4.3. Limitations

The index captures physical vulnerability and exposure but not adaptive capacity, so it is best read as a relative physical vulnerability index rather than a full risk assessment. The unweighted CVI computation assigns equal importance to all nine variables, an assumption that may not reflect their relative physical influence in the Volta Delta. It was, however, retained for comparability with prior assessments and to isolate the effect of subsidence inclusion. Because the index multiplies ranked variables, adding subsidence as a further

high-ranked component necessarily raises the composite value; the effect of subsidence is therefore assessed by comparing scenarios that share the same variables and scale, and by the resulting vulnerability-class and pattern changes, rather than by the magnitude of the index itself. Also, the 2 km by 2 km grid cells average out sub-kilometre variability, suppressing or smoothing localised value extremes of the nine variables. For instance, the grid cell means for the land subsidence variable peak at −4.23 mm/yr, although the highest point-scale rate measured was 7.68 mm/yr (Figure 3a), suggesting that the results are conservative. Lastly, the shoreline change estimate rests on two timestamps under the EPR approach and may not account for temporal variations between the timestamps. In the absence of tide monitoring stations in the delta, the study adopted SLR and tidal range inputs that are uniform alongshore and therefore do not contribute to spatial variability in the index. The InSAR rates are a 2016 to 2020 average and carry an anthropogenic component, including groundwater abstraction and salt mining, while regulation of the Volta River by the Akosombo dam has reduced fluvial sediment supply and natural aggradation; the temporal variability of these rates and the quantitative attribution of their drivers are beyond the present vulnerability assessment scope and are left to future monitoring with continuous GNSS and repeat InSAR.

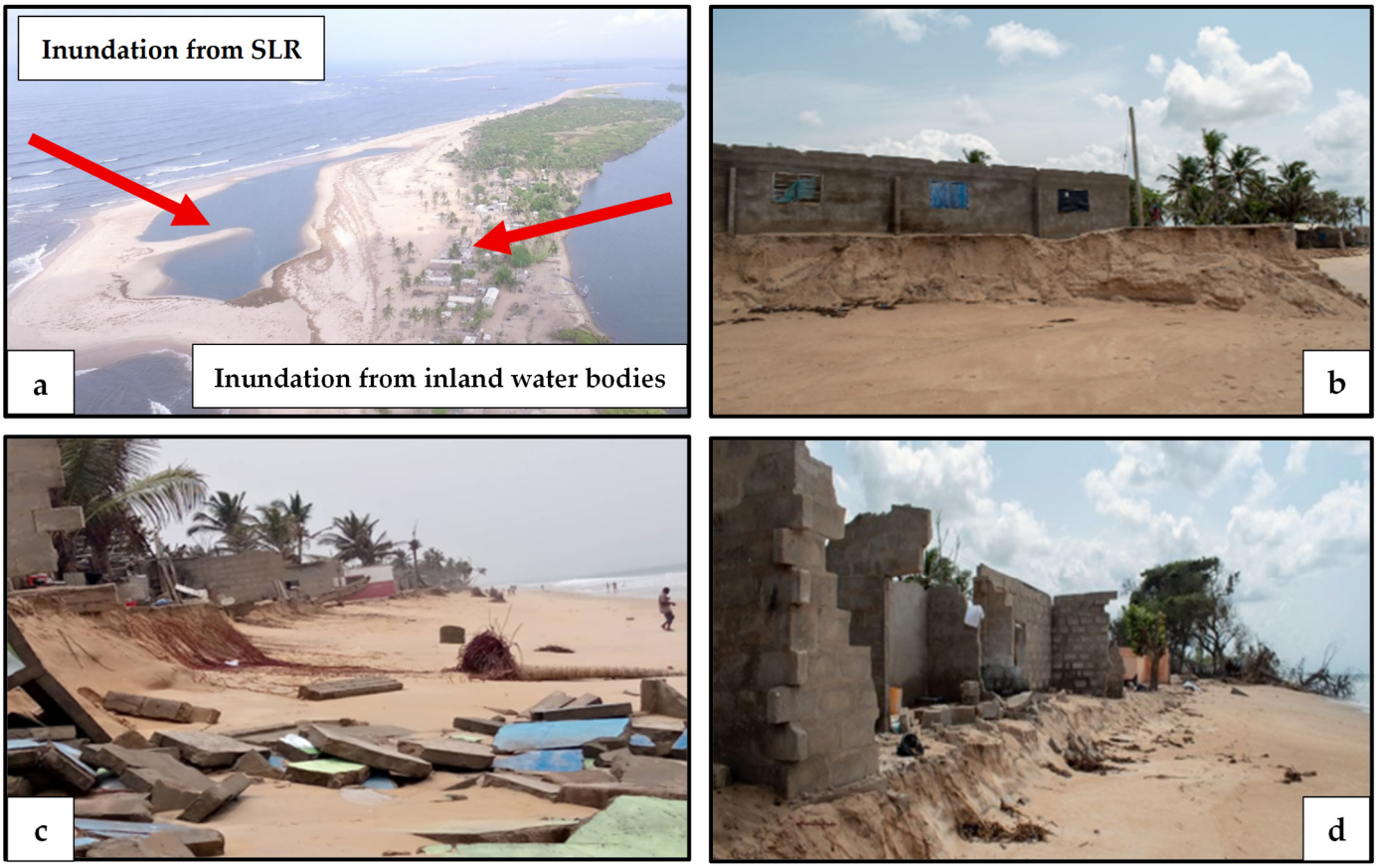


Figure 7. (**a**) Coastal narrowing along the Volta Delta's sand barrier, with forcings on both the seaward and landward boundaries (photo credit: Jayson-Quashigah). (**b**–**d**) Images showing destruction in coastal built-up areas due to coastal hazards (photo credit: Adogla-Bessa).

5. Conclusions

The study employed the use of an index-based approach that incorporated validated, InSAR-derived subsidence, the first of its kind in the Volta Delta, to assess the vulnerability and sensitivity of the delta's coastal areas to increasing coastal hazards. By computing three composite indices ($CVI_{+(v\text{-}sub)}$, $CVI_{+(u\text{-}sub)}$, and CVI_{sub}) across 72 contiguous grid

cells along the ~150 km coastline, and classifying all three against a common quantile distribution, the study isolates and quantifies the contribution of land subsidence to coastal vulnerability in a data-sparse deltaic setting.

Three findings stand out. First, the study showed that 75% of the entire coastline registered either high or very high vulnerability when spatially resolved local subsidence is included as an input variable. Across the three scenarios, the locally measured InSAR subsidence raised the share of the coast in the high or very high classes from 28% with no subsidence, through 44% under a regional AR6 estimate, to 75% under the spatially resolved measurement, and moved most cells at least one class up the scale without relocating the hotspots. This difference is consistent across all grid cells (Wilcoxon signed-rank test, $p < 0.001$), reported as a descriptive comparison rather than an independent statistical confirmation. Second, with measured mean subsidence of -3.35 mm/yr against the regional SLR of 4 to 5 mm/yr, the relative SLR experienced along the coast is approximately double the eustatic rate, a condition entirely missed by the assumed spatially uniform subsidence values used in earlier assessments. Higher subsidence rates will scale up the already compounding impacts of climate change further. Because subsidence adds directly to relative sea-level rise, the same compounding applies to any low-lying delta, so the framework, which is an assessment framework, transfers wherever validated, spatially resolved land-motion data are available. Third, vulnerability is spatially concentrated along the continuous stretch of sand barrier bounded by the two dominant lagoons, the Songor and Keta. These coastal margins (Keta especially) combine erodible geology, barrier beach geomorphology, built-up land cover, persistent subsidence and constrained retreat space, hence emerging as the delta's critical hotspots in every scenario.

These findings support the following recommendations: coastal management and adaptation planning should prioritise the identified hotspots for monitoring, early warning and contingency planning; instead of using global rates, validated InSAR-derived VLM must be adopted as a standard input in vulnerability frameworks by national agencies responsible for coastal assessment; regulatory attention should be directed at identifying and quantifying the human drivers of subsidence in the delta, such as groundwater abstraction and salt mining activities; hybrid defences that incorporate ecosystem-based measures should be adopted in place of hard engineering alone; and future research should test weighted CVI computations.

Supplementary Materials: The following supporting information can be downloaded at: https://www.mdpi.com/article/10.3390/rs18173042/s1, Table S1: Native resolution of each input variable and its assignment to a grid cell; Table S2: Data support at each cell size, where a cell is fully scored when all nine variables reach it; Figure S1: Coastal Vulnerability Index at four cell sizes, with the cell sizes showing vulnerability class on fixed index bands (a) and data completeness (b); Table S3: Composite CVI and vulnerability-class distribution for the three scenarios (72 cells); Figure S2: Spearman rank correlation of the alongshore CVI between the three scenarios (72 grid cells; rank 1 = least, 72 = most vulnerable); Table S4: Vulnerability-class transitions between each pair of scenarios (number of cells); Figure S3. Monte Carlo propagation of the InSAR subsidence uncertainty; Table S5: Per-cell InSAR statistics and Monte Carlo results (72 grid cells).

Author Contributions: Conceptualisation, S.Y.A., K.A.A., E.M., P.T., R.B. and P.S.J.M.; methodology, S.Y.A.; software, S.Y.A. and P.-N.J.-Q.; validation, S.Y.A., P.-N.J.-Q. and F.E.I.; formal analysis, S.Y.A. and P.-N.J.-Q.; investigation, S.Y.A.; resources, K.A.A., E.M. and P.T.; data curation, S.Y.A., P.-N.J.-Q., M.K.-B., O.O.O. and F.E.I.; writing—original draft preparation, S.Y.A., F.E.I. and O.O.O.; writing—review and editing, K.A.A., E.M., P.T., R.B. and P.S.J.M.; visualisation S.Y.A., P.-N.J.-Q. and F.E.I.; supervision, K.A.A., E.M., P.T., R.B. and P.S.J.M. All authors have read and agreed to the published version of the manuscript.

Funding: This study was partially funded by the Agence Française de Développement (AFD) [RE 726–2022 CZZ3340] within the framework of the ENGULF project.

Data Availability Statement: The data are contained within the article or Supplementary Materials. The Python pipeline used to compute and map the Coastal Vulnerability Index is publicly available on GitHub at https://github.com/selavorn/Automated-Coastal-Vulnerability-Index-Assessment, accessed on 2 September 2026.

Acknowledgments: During the preparation of this manuscript, the authors used Claude (v1.11187.5, Opus 4.8) for the purposes of generating the methodology workflow chart and general text improvement. The authors have reviewed and edited the output and take full responsibility for the content of this publication.

Conflicts of Interest: The authors declare no conflicts of interest.

Abbreviations

The following abbreviations are used in this manuscript:

AR6	IPCC Sixth Assessment Report
BGR	Bundesanstalt für Geowissenschaften und Rohstoffe
CS	Coastal Slope
CVI	Coastal Vulnerability Index
$CVI_{(-sub)}$	CVI without Subsidence
$CVI_{+(u-sub)}$	CVI with Spatially Uniform Regional Subsidence
$CVI_{+(v-sub)}$	CVI with Spatially Variable InSAR-Derived Local Subsidence
DEM	Digital Elevation Model
DSAS	Digital Shoreline Assessment System
DTM	Digital Terrain Model
ECMWF	European Centre for Medium-Range Weather Forecasts
EPR	End Point Rate
GIS	Geographic Information System
GL	Geology
GM	Geomorphology
GNSS	Global Navigation Satellite System
GPHA	Ghana Ports and Harbours Authority
GSA	Geological Survey Authority
InSAR	Interferometric Synthetic Aperture Radar
IPCC	Intergovernmental Panel on Climate Change
IW	Interferometric Wide
LULC	Land Use and Land Cover
MPS	Meridian Port Services
MTR	Mean Tidal Range
NASA	National Aeronautics and Space Administration
PS-InSAR	Persistent Scatterer Interferometric Synthetic Aperture Radar
S	Subsidence
S1	Sentinel-1
SAR	Synthetic Aperture Radar
SC	Shoreline Change
SLC	Single-Look Complex
SLR	Sea-Level Rise
SNAP	Sentinel Application Platform
SSP	Shared Socioeconomic Pathway
StaMPS	Stanford Method for Persistent Scatterers
SWH	Significant Wave Height
TRAIN	Toolbox for Reducing Atmospheric InSAR Noise

UTM	Universal Transverse Mercator
VLM	Vertical Land Motion
WGS	World Geodetic System

References

1. Nicholls, R.J.; Wong, P.P.; Burkett, V.; Codignotto, J.; Hay, J.; McLean, R.; Ragoonaden, S.; Woodroffe, C.D.; Abuodha, P.A.O.; Arblaster, J.; et al. Coastal Systems and Low-Lying Areas. In *Climate Change 2007: Impacts, Adaptation and Vulnerability. Contribution of Working Group II to the Fourth Assessment Report of the Intergovernmental Panel on Climate Change*; Cambridge University Press: Cambridge, UK; New York, NY, USA, 2007; pp. 315–356.
2. Durand, G.; van den Broeke, M.R.; Cozannet, G.L.; Edwards, T.L.; Holland, P.R.; Jourdain, N.C.; Marzeion, B.; Mottram, R.; Nicholls, R.J.; Pattyn, F.; et al. Sea-Level Rise: From Global Perspectives to Local Services. *Front. Mar. Sci.* **2022**, *8*, 709595. [CrossRef]
3. Neumann, B.; Vafeidis, A.T.; Zimmermann, J.; Nicholls, R.J. Future Coastal Population Growth and Exposure to Sea-Level Rise and Coastal Flooding—A Global Assessment. *PLoS ONE* **2015**, *10*, e0118571. [CrossRef] [PubMed]
4. Intergovernmental Panel on Climate Change (IPCC). *Climate Change 2021—The Physical Science Basis: Working Group I Contribution to the Sixth Assessment Report of the Intergovernmental Panel on Climate Change*, 1st ed.; Cambridge University Press: Cambridge, UK, 2023; ISBN 978-1-009-15789-6.
5. Avornyo, S.Y.; Minderhoud, P.S.J.; Teatini, P.; Seeger, K.; Hauser, L.T.; Woillez, M.-N.; Jayson-Quashigah, P.-N.; Mahu, E.; Kwame-Biney, M.; Appeaning Addo, K. The Contribution of Coastal Land Subsidence to Potential Sea-Level Rise Impact in Data-Sparse Settings: The Case of Ghana's Volta Delta. *Quat. Sci. Adv.* **2024**, *14*, 100175. [CrossRef]
6. Minderhoud, P.S.J.; Erkens, G.; Pham, V.H.; Bui, V.T.; Erban, L.; Kooi, H.; Stouthamer, E. Impacts of 25 Years of Groundwater Extraction on Subsidence in the Mekong Delta, Vietnam. *Environ. Res. Lett.* **2017**, *12*, 064006. [CrossRef] [PubMed]
7. Ohenhen, L.O.; Shirzaei, M.; Davis, J.L.; Tiwari, A.; Nicholls, R.; Dasho, O.; Sadhasivam, N.; Seeger, K.; Werth, S.; Chadwick, A.J.; et al. Global Subsidence of River Deltas. *Nature* **2026**, *649*, 894–901. [CrossRef] [PubMed]
8. Syvitski, J.P.M.; Kettner, A.J.; Overeem, I.; Hutton, E.W.H.; Hannon, M.T.; Brakenridge, G.R.; Day, J.; Vörösmarty, C.; Saito, Y.; Giosan, L.; et al. Sinking Deltas Due to Human Activities. *Nat. Geosci.* **2009**, *2*, 681–686. [CrossRef]
9. Wu, P.-C.; Wei, M.; D'Hondt, S. Subsidence in Coastal Cities Throughout the World Observed by InSAR. *Geophys. Res. Lett.* **2022**, *49*, e2022GL098477. [CrossRef]
10. Clark, P.U.; Shakun, J.D.; Marcott, S.A.; Mix, A.C.; Eby, M.; Kulp, S.; Levermann, A.; Milne, G.A.; Pfister, P.L.; Santer, B.D.; et al. Consequences of Twenty-First-Century Policy for Multi-Millennial Climate and Sea-Level Change. *Nat. Clim. Change* **2016**, *6*, 360–369. [CrossRef]
11. Xu, D.; Bisht, G.; Feng, D.; Tan, Z.; Li, L.; Qiu, H.; Leung, L.R. Impacts of Sea-Level Rise on Coastal Groundwater Table Simulated by an Earth System Model With a Land-Ocean Coupling Scheme. *Earth's Future* **2024**, *12*, e2024EF004479. [CrossRef]
12. Intergovernmental Panel on Climate Change (IPCC) Sea Level Rise and Implications for Low-Lying Islands, Coasts and Communities. In *The Ocean and Cryosphere in a Changing Climate: Special Report of the Intergovernmental Panel on Climate Change*; Cambridge University Press: Cambridge, UK, 2022; pp. 321–446.
13. Carnero-Bravo, V.; Sanchez-Cabeza, J.-A.; Ruiz-Fernández, A.C.; Merino-Ibarra, M.; Corcho-Alvarado, J.A.; Sahli, H.; Hélie, J.-F.; Preda, M.; Zavala-Hidalgo, J.; Díaz-Asencio, M.; et al. Sea Level Rise Sedimentary Record and Organic Carbon Fluxes in a Low-Lying Tropical Coastal Ecosystem. *CATENA* **2018**, *162*, 421–430. [CrossRef]
14. Nicholls, R. Planning for the Impacts of Sea Level Rise. *Oceanography* **2011**, *24*, 144–157. [CrossRef]
15. Avornyo, S.Y.; Addo, K.A.; Teatini, P.; Minderhoud, P.; Woillez, M.-N.; Jayson-Quashigah, P.-N.; Mahu, E. A Scoping Review of Coastal Vulnerability, Subsidence and Sea Level Rise in Ghana: Assessments, Knowledge Gaps and Management Implications. *Quat. Sci. Adv.* **2023**, *12*, 100108. [CrossRef]
16. Hauser, L.; Boni, R.; Minderhoud, P.-S.-J.; Teatini, P.; Woillez, M.-N.; Almar, R.; Avornyo, S.Y.; Addo, K.A. *A Scoping Study on Coastal Vulnerability to Relative Sea-Level Rise in the Gulf of Guinea*; Éditions AFD: Paris, France, 2023.
17. Appeaning Addo, K. Assessing Coastal Vulnerability Index to Climate Change: The Case of Accra—Ghana. *J. Coast. Res.* **2013**, *165*, 1892–1897. [CrossRef]
18. Nicholls, R.J.; Tol, R.S.J. Impacts and Responses to Sea-Level Rise: A Global Analysis of the SRES Scenarios over the Twenty-First Century. *Philos. Trans. R. Soc. A Math. Phys. Eng. Sci.* **2006**, *364*, 1073–1095. [CrossRef] [PubMed]
19. Dada, O.A.; Almar, R.; Morand, P. Coastal Vulnerability Assessment of the West African Coast to Flooding and Erosion. *Sci. Rep.* **2024**, *14*, 890. [CrossRef] [PubMed]
20. Nyadzi, E.; Bessah, E.; Kranjac-Berisavljevic, G. Taking Stock of Climate Change Induced Sea Level Rise across the West African Coast. *Environ. Claims J.* **2021**, *33*, 77–90. [CrossRef]

21. Bonì, R.; Minderhoud, P.S.J.; Addo, K.A.; Avornyo, S.Y.; Hauser, L.T.; Ikuemonisan, F.E.; Woillez, M.-N.; Canesi, M.; Wade, C.T.; Almar, R.; et al. Sixty Years of Research on Land Subsidence and Sea-Level Change: A Systematic Review of Global Literature with a Regional Lens on the Gulf of Guinea, Africa. *Land* **2026**, *15*, 721. [CrossRef]
22. Chaussard, E.; Amelung, F.; Abidin, H.; Hong, S.-H. Sinking Cities in Indonesia: ALOS PALSAR Detects Rapid Subsidence Due to Groundwater and Gas Extraction. *Remote Sens. Environ.* **2013**, *128*, 150–161. [CrossRef]
23. Gambolati, G.; Teatini, P. Geomechanics of Subsurface Water Withdrawal and Injection. *Water Resour. Res.* **2015**, *51*, 3922–3955. [CrossRef]
24. Shirzaei, M.; Bürgmann, R. Global Climate Change and Local Land Subsidence Exacerbate Inundation Risk to the San Francisco Bay Area. *Sci. Adv.* **2018**, *4*, eaap9234. [CrossRef] [PubMed]
25. Fowler, A.; Ng, F. *Glaciers and Ice Sheets in the Climate System*; Springer International Publishing: Cham, Switzerland, 2021; ISBN 978-3-030-42582-1.
26. Koster, K.; Stafleu, J.; Cohen, K.M.; Stouthamer, E.; Busschers, F.S.; Middelkoop, H. Three-Dimensional Distribution of Organic Matter in Coastal-Deltaic Peat: Implications for Subsidence and Carbon Dioxide Emissions by Human-Induced Peat Oxidation. *Anthropocene* **2018**, *22*, 1–9. [CrossRef]
27. Stouthamer, E.; Asselen, S. van Drivers of Delta Subsidence. In *Proceedings of the Abstract from 36th IAHR World Congress on Deltas of the Future*; IAHR: Delft, The Netherlands, 2015.
28. Bukvic, A.; Rohat, G.; Apotsos, A.; Sherbinin, A. de A Systematic Review of Coastal Vulnerability Mapping. *Sustainability* **2020**, *12*, 2822. [CrossRef]
29. Boateng, I.; Wiafe, G.; Jayson-Quashigah, P.-N. Mapping Vulnerability and Risk of Ghana's Coastline to Sea Level Rise. *Mar. Geod.* **2017**, *40*, 23–39. [CrossRef]
30. Theocharidis, C.; Doukanari, M.; Kalogirou, E.; Christofi, D.; Mettas, C.; Kontoes, C.; Hadjimitsis, D.; Argyriou, A.V.; Eliades, M. Coastal Vulnerability Index (CVI) Assessment: Evaluating Risks Associated with Human-Made Activities along the Limassol Coastline, Cyprus. *Remote Sens.* **2024**, *16*, 3688. [CrossRef]
31. Babanawo, D.; Mattah, P.A.D.; Agblorti, S.K.M.; Brempong, E.K.; Mattah, M.M.; Aheto, D.W. Local Indicator-Based Flood Vulnerability Indices and Predictors of Relocation in the Ketu South Municipal Area of Ghana. *Sustainability* **2022**, *14*, 5698. [CrossRef]
32. Torresan, S.; Critto, A.; Rizzi, J.; Zabeo, A.; Furlan, E.; Marcomini, A. DESYCO: A Decision Support System for the Regional Risk Assessment of Climate Change Impacts in Coastal Zones. *Ocean Coast. Manag.* **2016**, *120*, 49–63. [CrossRef]
33. Hinkel, J.; Klein, R.J.T. Integrating Knowledge to Assess Coastal Vulnerability to Sea-Level Rise: The Development of the DIVA Tool. *Glob. Environ. Change* **2009**, *19*, 384–395. [CrossRef]
34. Ružić, I.; Jovančević, S.D.; Benac, Č.; Krvavica, N. Assessment of the Coastal Vulnerability Index in an Area of Complex Geological Conditions on the Krk Island, Northeast Adriatic Sea. *Geosciences* **2019**, *9*, 219. [CrossRef]
35. Beattie, A.; Ahmed, M.; Chu, T.; Gebremichael, E.; Elshalkany, M.; Abdelrehim, R. Temporal Gravimetry, Campaign and Permanent GNSS, and Interferometric Radar Techniques: A Comparative Approach to Quantifying Land Deformation Rates in Coastal Texas. *Sci. Total Environ.* **2024**, *956*, 177280. [CrossRef] [PubMed]
36. Fabris, M.; Battaglia, M.; Chen, X.; Menin, A.; Monego, M.; Floris, M. An Integrated InSAR and GNSS Approach to Monitor Land Subsidence in the Po River Delta (Italy). *Remote Sens.* **2022**, *14*, 5578. [CrossRef]
37. Rossi, G. L'érosion Du Littoral Dans Le Golfe Du Bénin: Un Exemple de Perturbation d'un Équilibre Morphodynamique. *Z. Geomorphol.* **1989**, *73*, 139–165.
38. Jayson-Quashigah, P.-N.; Addo, K.A.; Kodzo, K.S. Medium Resolution Satellite Imagery as a Tool for Monitoring Shoreline Change. Case Study of the Eastern Coast of Ghana. *J. Coast. Res.* **2013**, *65*, 511–516. [CrossRef]
39. Kumapley, N.K. The Geology and Geotechnology of the Keta Basin with Particular Reference to Coastal Protection. In *Coastal Lowlands*; Springer: Dordrecht, The Netherlands, 1989; pp. 311–320.
40. Jayson-Quashigah, P.-N.; Addo, K.A.; Amisigo, B.; Wiafe, G. Assessment of Short-Term Beach Sediment Change in the Volta Delta Coast in Ghana Using Data from Unmanned Aerial Vehicles (Drone). *Ocean Coast. Manag.* **2019**, *182*, 104952. [CrossRef]
41. Appeaning Addo, K.; Nicholls, R.J.; Codjoe, S.N.A.; Abu, M. A Biophysical and Socioeconomic Review of the Volta Delta, Ghana. *J. Coast. Res.* **2018**, *345*, 1216–1226. [CrossRef]
42. Gornitz, V. Global Coastal Hazards from Future Sea Level Rise. *Palaeogeogr. Palaeoclimatol. Palaeoecol.* **1991**, *89*, 379–398. [CrossRef]
43. Thieler, E.R.; Hammar-Klose, E.S. *National Assessment of Coastal Vulnerability to Sea-Level Rise: Preliminary Results for the U.S. Pacific Coast*; USGS Report: Reston, VA, USA, 2000.
44. Fox-Kemper, B.; Hewitt, H.; Xiao, C.; Aðalgeirsdóttir, G.; Drijfhout, S.; Edwards, T.; Golledge, N.; Hemer, M.; Kopp, R.; Krinner, G.; et al. Ocean, Cryosphere and Sea Level Change. In *Climate Change 2021—The Physical Science Basis*; Cambridge University Press: Cambridge, UK, 2021; pp. 1211–1362.

45. Kopp, R.E.; Garner, G.G.; Hermans, T.H.J.; Jha, S.; Kumar, P.; Reedy, A.; Slangen, A.B.A.; Turilli, M.; Edwards, T.L.; Gregory, J.M.; et al. The Framework for Assessing Changes To Sea-Level (FACTS) v1.0: A Platform for Characterizing Parametric and Structural Uncertainty in Future Global, Relative, and Extreme Sea-Level Change. *Geosci. Model Dev.* **2023**, *16*, 7461–7489. [CrossRef]
46. Garner, G.G.; Hermans, T.; Kopp, R.E.; Slangen, A.B.A.; Edwards, T.L.; Levermann, A.; Nowicki, S.; Palmer, M.D.; Smith, C.; Fox-Kemper, B.; et al. *IPCC AR6 Sea Level Projections 2021*; Zenodo: Geneva, Switzerland, 2021.
47. Athanasiou, P.; Van Dongeren, A.; Pronk, M.; Giardino, A.; Vousdoukas, M.; Ranasinghe, R. Global Coastal Characteristics (GCC): A Global Dataset of Geophysical, Hydrodynamic, and Socioeconomic Coastal Indicators. *Earth Syst. Sci. Data* **2024**, *16*, 3433–3452. [CrossRef]
48. Pronk, M.; Hooijer, A.; Eilander, D.; Haag, A.; De Jong, T.; Vousdoukas, M.; Vernimmen, R.; Ledoux, H.; Eleveld, M. DeltaDTM: A Global Coastal Digital Terrain Model. *Sci. Data* **2024**, *11*, 273. [CrossRef] [PubMed]
49. Geological Survey Authority, Accra, Ghana (GSA). *Bundesanstalt für Geowissenschaften und Rohstoffe (BGR) Geological Map of Ghana 2009*; Geological Survey Department (GSD): Accra, Ghana, 2009.
50. Giardino, A.; Schrijvershof, R.; Nederhoff, C.M.; de Vroeg, H.; Brière, C.; Tonnon, P.K.; Caires, S.; Walstra, D.J.; Sosa, J.; van Verseveld, W.; et al. A Quantitative Assessment of Human Interventions and Climate Change on the West African Sediment Budget. *Ocean Coast. Manag.* **2018**, *156*, 249–265. [CrossRef]
51. Karra, K.; Kontgis, C.; Statman-Weil, Z.; Mazzariello, J.C.; Mathis, M.; Brumby, S.P. Global Land Use/Land Cover with Sentinel 2 and Deep Learning. In *Proceedings of the 2021 IEEE International Geoscience and Remote Sensing Symposium IGARSS*; IEEE: Brussels, Belgium, 2021; pp. 4704–4707.
52. Delgado Blasco, J.M.; Ziemer, J.; Foumelis, M.; Dubois, C. *SNAP2StaMPS v2: Increasing Features and Supported Sensors in the Open Source SNAP2StaMPS Processing Scheme 2023*; Zenodo: Geneva, Switzerland, 2023.
53. Bekaert, D.P.S.; Walters, R.J.; Wright, T.J.; Hooper, A.J.; Parker, D.J. Statistical Comparison of InSAR Tropospheric Correction Techniques. *Remote Sens. Environ.* **2015**, *170*, 40–47. [CrossRef]
54. Noor, N.M.; Maulud, K.N.A. Coastal Vulnerability: A Brief Review on Integrated Assessment in Southeast Asia. *J. Mar. Sci. Eng.* **2022**, *10*, 595. [CrossRef]
55. Husnayaen; Rimba, A.B.; Osawa, T.; Parwata, I.N.S.; As-syakur, A.R.; Kasim, F.; Astarini, I.A. Physical Assessment of Coastal Vulnerability under Enhanced Land Subsidence in Semarang, Indonesia, Using Multi-Sensor Satellite Data. *Adv. Space Res.* **2018**, *61*, 2159–2179. [CrossRef]
56. Thieler, E.R.; Himmelstoss, E.A.; Zichichi, J.L.; Ergul, A. *The Digital Shoreline Analysis System (DSAS) Version 4.0—An ArcGIS Extension for Calculating Shoreline Change*; U.S. Geological Survey: Reston, VA, USA, 2009.
57. Gornitz, V.M.; Daniels, R.C.; White, T.W.; Birdwell, K.R. The Development of a Coastal Risk Assessment Database: Vulnerability to Sea-Level Rise in the U.S. Southeast. *Coast. Res.* **1994**, *12*, 327–338.
58. Koroglu, A.; Ranasinghe, R.; Jiménez, J.A.; Dastgheib, A. Comparison of Coastal Vulnerability Index Applications for Barcelona Province. *Ocean Coast. Manag.* **2019**, *178*, 104799. [CrossRef]
59. Gornitz, V.; Kanciruk, P. Assessment of Global Coastal Hazards from Sea Level Rise. In *Proceedings of Coastal Zone 89, 6th Symposium on Coastal and Ocean Management*; ASCE: Charleston, SC, USA, 1989; pp. 1345–1359.
60. Thieler, E.R.; Hammar-Klose, S. *National Assessment of Coastal Vulnerability to Sea-Level Rise: Preliminary Results for the U.S. Atlantic Coast*; U.S. Geological Survey Open-File Report 99-593; U.S. Geological Survey: Woods Hole, MA, USA, 1999.
61. Oloyede, M.O.; Williams, A.B.; Ode, G.O.; Benson, N.U. Coastal Vulnerability Assessment: A Case Study of the Nigerian Coastline. *Sustainability* **2022**, *14*, 2097. [CrossRef]
62. Mahapatra, M.; Ramakrishnan, R.; Rajawat, A.S. Coastal Vulnerability Assessment of Gujarat Coast to Sea Level Rise Using GIS Techniques: A Preliminary Study. *J. Coast. Conserv.* **2015**, *19*, 241–256. [CrossRef]
63. Tanim, A.H.; Goharian, E.; Moradkhani, H. Integrated Socio-Environmental Vulnerability Assessment of Coastal Hazards Using Data-Driven and Multi-Criteria Analysis Approaches. *Sci. Rep.* **2022**, *12*, 11625. [CrossRef] [PubMed]
64. López Royo, M.; Ranasinghe, R.; Jiménez, J.A. A Rapid, Low-Cost Approach to Coastal Vulnerability Assessment at a National Level. *J. Coast. Res.* **2016**, *320*, 932–945. [CrossRef]
65. Pendleton, E.A.; Barras, J.A.; Williams, S.J.; Twichell, D.C. *Coastal Vulnerability Assessment of the Northern Gulf of Mexico to Sea-Level Rise and Coastal Change*; U.S. Geological Survey: Woods Hole, USA, 2010.
66. Mclaughlin, S.; Cooper, J.A.G. A Multi-Scale Coastal Vulnerability Index: A Tool for Coastal Managers? *Environ. Hazards* **2010**, *9*, 233–248. [CrossRef]
67. Gornitz, V. *Vulnerability of the East Coast, U.S.A. to Future Sea Level Rise*; Coastal Education & Research Foundation, Inc.: Earlysville, VA, USA, 1990; pp. 201–237. Available online: https://www.jstor.org/stable/44868636 (accessed on 2 September 2026).
68. Amenuvor, M.; Gao, W.; Li, D.; Shao, D. Effects of Dam Regulation on the Hydrological Alteration and Morphological Evolution of the Volta River Delta. *Water* **2020**, *12*, 646. [CrossRef]
69. Boateng, I.; Bray, M.; Hooke, J. Estimating the Fluvial Sediment Input to the Coastal Sediment Budget: A Case Study of Ghana. *Geomorphology* **2012**, *138*, 100–110. [CrossRef]

70. Fiadzigbey, M. The Story of Keta: The Land Factor. *Volta Monit.* **2005**, 20–22.
71. Pontee, N. Defining Coastal Squeeze: A Discussion. *Ocean Coast. Manag.* **2013**, *84*, 204–207. [CrossRef]
72. Doody, J.P. Coastal Squeeze and Managed Realignment in Southeast England, Does It Tell Us Anything about the Future? *Ocean Coast. Manag.* **2013**, *79*, 34–41. [CrossRef]
73. Yidana, S.M.; Banoeng-Yakubo, B.; Akabzaa, T.M. Analysis of Groundwater Quality Using Multivariate and Spatial Analyses in the Keta Basin, Ghana. *J. Afr. Earth Sci.* **2010**, *58*, 220–234. [CrossRef]

Disclaimer/Publisher's Note: The statements, opinions and data contained in all publications are solely those of the individual author(s) and contributor(s) and not of MDPI and/or the editor(s). MDPI and/or the editor(s) disclaim responsibility for any injury to people or property resulting from any ideas, methods, instructions or products referred to in the content.